Delft University of Technology

MS-GIFT

Multi-Sided Geometry-Independent Field ApproximaTion Approach for Isogeometric Analysis

Wang, Meng Yun; Ji, Ye; Lan, Lin; Zhu, Chun Gang

Important note
To cite this publication, please use the final published version (if applicable).
Please check the document version above.

MS-GIFT: Multi-Sided Geometry-Independent Field ApproximaTion Approach for Isogeometric Analysis

Meng-Yun Wang [a,b], Ye Ji [c], Lin Lan [a,b], Chun-Gang Zhu [a,b,*]

[a] *School of Mathematical Sciences, Dalian University of Technology, Dalian 116024, China*
[b] *Key Laboratory for Computational Mathematics and Data Intelligence of Liaoning Province, Dalian University of Technology, Dalian, 116024, Liaoning, China*
[c] *Delft Institute of Applied Mathematics, Delft University of Technology, Delft, 2628CD, the Netherlands*

ARTICLE INFO

ABSTRACT

The Geometry-Independent Field approximaTion (GIFT) technique, an extension of isogeometric analysis (IGA), allows for separate spaces to parameterize the computational domain and approximate solution field. Based on the GIFT approach, this paper proposes a novel IGA methodology that incorporates toric surface patches for multi-sided geometry representation, while utilizing B-spline or truncated hierarchical B-spline (THB-spline) basis for analysis. By creating an appropriate bijection between the parametric domains of distinct bases for modeling and approximation, our method ensures smoothness within the computational domain and combines the compact support of B-splines or the local refinement potential of THB-splines, resulting in more efficient and precise solutions. To enhance the quality of parameterization and consequently boost the accuracy of downstream analysis, we suggest optimizing the composite toric parameterization. Numerical examples validate the effectiveness and superiority of our suggested approach.

1. Introduction

Isogeometric analysis (IGA) [1,2] is a computational methodology designed to establish a direct connection between Computer-Aided Design (CAD) and Finite Element Analysis (FEA). The fundamental concept of IGA involves using the same spline-based representations, such as non-uniform rational B-splines (NURBS), for both geometry representation and simulation analysis. With the extensive use of spline tools in CAD systems, IGA based on this approach has consequently gained significant traction [3–5].

Although NURBS are effective in representing 4-sided domains, their use in parameterizing multi-sided computational domains may result in a loss of smoothness or even bijectivity, due to the inherent limitations of their tensor product definition [6]. To tackle this issue, one solution is to utilize a multi-patch configuration [7–9]. Wang et al. [10] propose a deep learning framework, named IGA-Reuse-Net, for efficient reuse of numerical simulations on topology-consistent models. Furthermore, Pan et al. introduce subdivision-based IGA methods for complex surfaces [11,12]. In the realm of volumetric modeling, two interpolatory Catmull–Clark volumetric subdivision methods are proposed [13]. Xu et al. propose a r-refinement framework by using Winslow's mapping and monitor function approach [14]. Another solution is to adopt multi-sided geometry modeling tools with single-patch structures [15,16].

Toric surface patches, introduced by Krasauskas [17] as a generalization of rational Bézier surfaces, offer a solution to this challenge. By employing a specific definition over arbitrary convex polygonal integer lattice sets, toric surfaces have been widely investigated [18,19] where showcase their potential in constructing suitable parameterizations for IGA, resulting in impressive performance [20].

Refinement is a powerful technique for enhancing numerical accuracy by increasing degrees-of-freedom (DOFs). To accomplish this, geometric algorithms are commonly adopted, such as h-refinement through knot insertion, p-refinement via degree elevation, and k-refinement combining both methods. However, the refinement strategies for toric surface patches exhibit certain limitations. Li et al. [21] introduce a p-refinement for toric surface patches that spans the entire domain, resulting in a dense stiffness matrix. Moreover, the potential rapid increase in the stiffness matrix's condition number adversely impacts the numerical stability of the IGA solution. In contrast, the h-refinement for toric surface patches proposed by Ji et al. [15] addresses this issue and offers a more stable numerical solution, but at the expense of diminished high-order continuity. These limitations present considerable obstacles for IGA using toric surface patches.

Geometry-Independent Field approximaTion (GIFT) is a powerful and versatile generalization of IGA [22,23]. The primary concept behind GIFT is to facilitate the utilization of distinct and separate spaces
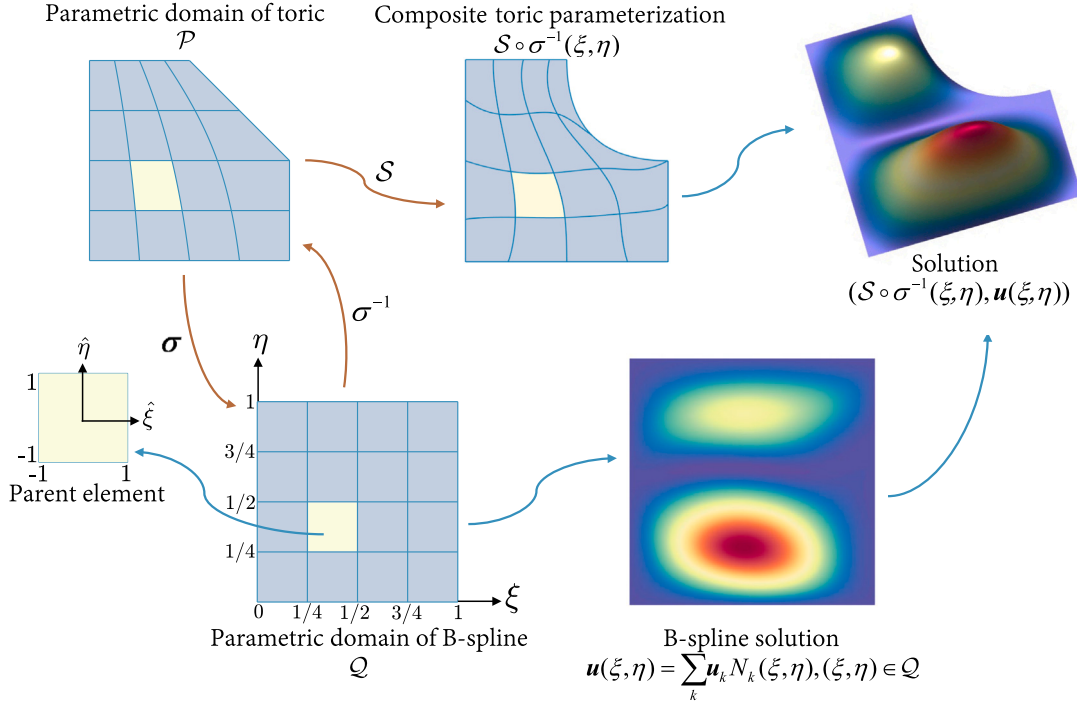

Fig. 1. Schematic illustration of our Multi-Sided Geometry-Independent Field approximaTion (MS-GIFT) method.

for parameterizing the computational domain and approximating the solution field. This decoupling offers several key benefits. Firstly, it enables the use of basis functions specifically tailored to the requirements of the problem, leading to improved accuracy in the solution approximation. Secondly, it allows for greater adaptivity in the numerical solution process, as the refinement strategies can be independently tailored to both the geometry and solution field. This can lead to a more accurate approximation of the solution with fewer degrees of freedom, ultimately resulting in faster computations and reduced memory requirements.

Building upon the GIFT approach, we incorporate toric surface patches to represent multi-sided computational domains and utilize B-spline or truncated hierarchical B-spline (THB-spline) basis functions as the solution basis for analysis, and then propose the multi-sided GIFT (MS-GIFT) method for IGA. This method not only preserves the exact geometry representation and smoothness within the polygonal computational domain but also capitalizes on the local support of B-splines or the local refinement capabilities of THB-splines, leading to more efficient and accurate solutions.

Achieving this, however, is not a straightforward task. Fig. 1 shows the graphical overview of our proposed MS-GIFT method. The primary challenge arises from the fact that the parametric domains of bivariate B-spline and THB-spline are typically rectangular (for simplicity, chosen as the unit square in this paper), while the parametric domains of toric surface patches are polygonal. Consequently, it is crucial to establish an appropriate bijection σ between these two parametric domains. Additionally, the quality of the parameterization plays a vital role in the accuracy and efficiency of the subsequent analysis. To tackle this issue, we optimize the composite toric parameterization $\mathcal{S} \circ \sigma^{-1}$ by making adjustments to the inner control points and weights as required. This optimization process aims to enhance the performance of our method in various applications. Numerical examples validate the effectiveness of our approach, as they show that it achieves high accuracy and excellent continuity within the resulting numerical solutions. These results highlight the potential of this method in a wide range of applications, particularly in scenarios where traditional methods may fall short.

Our main contributions are summarized as follows:

(1) We establish an appropriate bijection between polygonal and square parametric domains, along with two methods for calculating its inverse mapping. This mapping is then utilized to create a connection between the geometric basis and the solution basis, facilitating the integration of different spaces.

(2) We introduce the concept of composite parameterization optimization, which significantly mitigates the deformation issues arising from the mapping between parametric domains, ensuring a higher-quality geometric representation and analysis.

(3) By modeling multi-sided surfaces and utilizing basis functions with local support or local refinement capabilities, we avoid the destabilization problems caused by the p-refinement of toric methods in IGA. This approach introduces locality to multi-sided surface methods, enhancing the overall efficiency and accuracy of the computational process.

2. Preliminaries

This section offers a succinct introduction to toric surface patches, B-splines, truncated hierarchical B-splines (THB-splines), and Wachspress barycentric coordinates, primarily to fix the relevant notations. For further details, interested readers may refer to [17,24–26].

2.1. Toric surface patches

Let $\mathcal{A} \subset \mathbb{Z}^2$ denote a set of integer lattice points with an N-sided polygonal convex hull, represented as $\Delta_{\mathcal{A}}$. It can be defined as

$$\Delta_{\mathcal{A}} = \{(u, v) \in \mathbb{R}^2 \mid L_i(u, v) \geq 0, i = 1, 2, \ldots, N\},$$

where $L_i(u, v) = a_i u + b_i v + c_i$ is the equation of the ith edge Γ_i of $\Delta_{\mathcal{A}}$, and a_i, b_i, c_i are coprime integers. Then we have the following definition of toric surface patches:

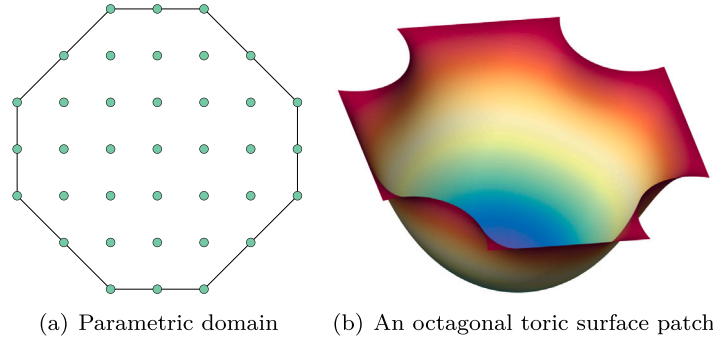(a) Parametric domain   (b) An octagonal toric surface patch

Fig. 2. An example of toric surface patch.

Definition 1 ([17]). Given a finite set of lattice points $\mathcal{A}$, let its N-sided polygonal convex hull be denoted as $\Delta_{\mathcal{A}}$. A toric surface patch is then defined as the image of the rational mapping: $S : \Delta_{\mathcal{A}} \to \mathbb{R}^3$

$$S(u,v) = \frac{\sum_{\mathbf{a} \in \mathcal{A}} \omega_{\mathbf{a}} \mathbf{P}_{\mathbf{a}} \beta_{\mathbf{a}}(u,v)}{\sum_{\mathbf{a} \in \mathcal{A}} \omega_{\mathbf{a}} \beta_{\mathbf{a}}(u,v)}, \quad (u,v) \in \Delta_{\mathcal{A}}, \tag{1}$$

where $\mathbf{P}_{\mathbf{a}} \in \mathbb{R}^3$ is the control point, $\omega_{\mathbf{a}} > 0$ is the weight corresponding to the control point $\mathbf{P}_{\mathbf{a}}$, $\Delta_{\mathcal{A}}$ is referred to as the parametric domain, and

$$\beta_{\mathbf{a}}(u,v) = c_{\mathbf{a}} \prod_{i=1}^{N} L_i(u,v)^{L_i(\mathbf{a})}$$

is the toric-Bernstein basis function for the lattice point $\mathbf{a}$, where $c_{\mathbf{a}} > 0$ is a coefficient.

For instance, a set of lattice points and its corresponding octagonal convex hull are illustrated in Fig. 2(a). Additionally, an octagonal toric surface patch is defined within this parametric domain, as depicted in Fig. 2(b).

2.2. B-splines and truncated hierarchical B-splines

B-splines, piecewise-defined polynomial functions, exhibit desirable properties such as local support, smoothness, and computational efficiency. They are frequently employed in curve and surface approximation for computer-aided geometric design (CAGD), computer graphics, and a variety of engineering applications.

An univariate B-spline basis function of degree p is defined over a non-decreasing knot vector $\Xi = \{\xi_i\}_{i=0}^{m}$. The B-spline basis functions are determined using the recursive Cox-de Boor formula:

$$\hat{N}_i^p(\xi) = \frac{\xi - \xi_i}{\xi_{i+p} - \xi_i} \hat{N}_i^{p-1}(\xi) + \frac{\xi_{i+p+1} - \xi}{\xi_{i+p+1} - \xi_{i+1}} \hat{N}_{i+1}^{p-1}(\xi), \tag{2}$$

starting from

$$\hat{N}_i^0(\xi) = \begin{cases} 1, & \text{if } \xi \in [\xi_i, \xi_{i+1}), \\ 0, & \text{otherwise,} \end{cases}$$

where ratios of the form $0/0$ are defined as zero.

Extending to bivariate B-spline basis functions is straightforward. Given two knot vectors Ξ and $\mathcal{H}$ in the ξ- and η-directions, respectively, bivariate B-spline basis functions are computed using the product of the univariate B-spline basis functions:

$$N_{i,j}^{p,q}(\xi,\eta) = N_i^p(\xi) N_j^q(\eta). \tag{3}$$

THB-splines are a generalization of B-splines that offer an efficient approach for local refinement of basis functions. Given a sequence of nested domains $\hat{\Omega}^0 \supseteq \hat{\Omega}^1 \supseteq \dots \supseteq \hat{\Omega}^M$, each domain $\hat{\Omega}^k$ comprises axis-aligned meshes, as illustrated in Fig. 3(a), the hierarchical B-spline (HB-spline) basis functions $\hat{\mathfrak{H}}$ are then defined as:

$$\hat{\mathfrak{H}} = \bigcup_{l=0,1,\dots,M-1} \{ N_{i,j}^{p,q} \in \hat{\mathfrak{B}}^l : \tag{4}$$

$$\text{supp}\left(N_{i,j}^{p,q}\right) \subset \hat{\Omega}^l \wedge \text{supp}\left(N_{i,j}^{p,q}\right) \not\subset \hat{\Omega}^{l+1} \},$$

where $\hat{\mathfrak{B}}^l$ represents the B-spline space spanned by B-spline basis functions at level l, and $\text{supp}\left(N_{i,j}^{p,q}\right)$ denotes the intersection of the support of $N_{i,j}^{p,q}$ with $\hat{\Omega}^0$.

However, the HB-spline basis functions lack the property of partition of unity. To address this issue, THB-spline basis functions are defined by iteratively applying the truncation operator to all basis functions in $\hat{\mathfrak{H}}$:

$$\hat{\mathfrak{T}} = \left\{ \text{Trunc}^{l+1}\left(N_{i,j}^{p,q}\right) : N_{i,j}^{p,q} \in \hat{\mathfrak{H}} \bigcap \hat{\mathfrak{B}}^l \right\} \cup \left\{ N_{i,j}^{p,q} \in \hat{\mathfrak{B}}^{l+1} : supp\left(N_{i,j}^{p,q}\right) \subset \hat{\Omega}^{l+1} \right\}, \tag{5}$$

where $\text{Trunc}^l := \text{trunc}^{M-1}\left(\text{trunc}^{M-2} \cdots \left(\text{trunc}^{l+1}\beta\right) \cdots\right)$, and $\text{trunc}^{l+1}\beta := \sum_{\beta \in \hat{\mathfrak{B}}^{l+1}, supp(\beta) \not\subset \hat{\Omega}^{l+1}} c_{\beta}^{l+1} \beta$. Fig. 3(b) illustrates bivariate THB-spline basis functions defined over nested domains in Fig. 3(a).

2.3. Wachspress barycentric coordinates

Wachspress barycentric coordinates [26] are a type of generalized barycentric coordinates used for interpolating values over convex polygons. An alternative expression can be found in [27].

Definition 2 ([27]). Given an N-sided convex polygonal domain $\mathcal{P}$ with vertices denoted as $\mathbf{v}_1, \mathbf{v}_2, \dots, \mathbf{v}_N$ ($N \geq 4$). For each side $\Gamma_i = \overline{\mathbf{v}_{i-1} \mathbf{v}_i}$, let the outward unit normal be $\mathbf{n}_i = (n_1^i, n_2^i)^{\text{T}}$. Define $g_i^{\perp}(u)$ as the perpendicular distance of u to the edge Γ_i:

$$g_i^{\perp}(u) = (\mathbf{v}_i - u) \cdot \mathbf{n}_i, \quad \forall u = (u,v)^{\text{T}} \in \mathcal{P}.$$

Wachspress barycentric coordinates can be represented as follows:

$$\lambda_i(u) = \frac{w_i(u)}{\sum_{j=1}^{N} w_j(u)}, \quad i = 1, 2, \dots, N, \tag{6}$$

where

$$w_i(u) := \frac{\mathbf{n}_{i-1} \times \mathbf{n}_i}{g_{i-1}^{\perp}(u) g_i^{\perp}(u)},$$

and $\mathbf{n}_{i-1} \times \mathbf{n}_i = n_1^{i-1} n_2^i - n_2^{i-1} n_1^i$. For indices exceeding the specified range, we impose the conditions: $\mathbf{v}_0 = \mathbf{v}_n$, $g_0^{\perp}(u) = g_n^{\perp}(u)$ and $\mathbf{n}_0 = \mathbf{n}_n$.

The gradients of Wachspress barycentric coordinates (6) can be calculated by

$$\nabla_u \lambda_i = \lambda_i \left(\mathbf{R}_i - \sum_{j=1}^{n} \lambda_j \mathbf{R}_j\right), \tag{7}$$

where $\nabla_u = (\frac{\partial}{\partial u}, \frac{\partial}{\partial v})^{\text{T}}$, and

$$\mathbf{R}_i(\mathbf{x}) = \frac{\mathbf{n}_{i-1}}{g_{i-1}^{\perp}(\mathbf{x})} + \frac{\mathbf{n}_i}{g_i^{\perp}(\mathbf{x})}.$$

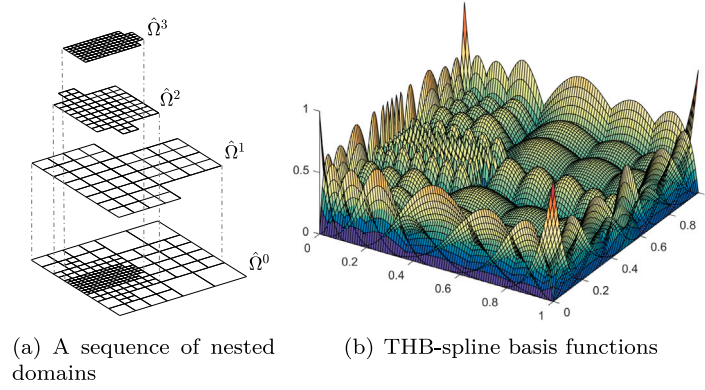(a) A sequence of nested domains   (b) THB-spline basis functions

Fig. 3. A sequence of nested domains for the construction of the spline hierarchy and its corresponding THB-spline basis functions.

3. Composite toric parameterization

Constructing analysis-suitable parameterizations from the boundary representation (B-Rep) of a physical domain Ω is an essential preprocessing step in the IGA pipeline. Within this context, "analysis-suitable" parameterizations are characterized by bijective mappings that exhibit good orthogonality and uniformity. The quality of such parameterizations is known to profoundly influence the numerical stability and accuracy of subsequent analyses, as pointed out in the literature [6,28,29].

However, unlike traditional IGA and GIFT approaches that rely on quadrilateral parametric domains, our MS-GIFT scheme employs polygonal parametric domains using toric surface patches, as shown in Fig. 1. That way, the quality of the composite toric parameterization $\mathcal{S} \circ \sigma^{-1}$ becomes crucial. Consequently, a bijection between a polygonal domain (the parametric domain of a toric surface patch) and a square domain (the parametric domain of a B-spline basis) is mandatory. To address this, we first consider the bijective mapping between parametric domains in Section 3.1 and subsequently enhance the quality of the composite toric parameterization in Section 3.2.

3.1. Bijective mapping between geometric and analysis parametric domains

As mentioned in Section 2.1, the parametric domain $\Delta_{\mathcal{A}} = \mathcal{P}$ of a toric surface patch is an N-sided polygon, whereas the parameterization $\mathcal{Q}$ corresponds to a unit square. Consequently, the initial step entails establishing a bijective mapping σ between the parametric domain $\mathcal{P}$ of the toric surface patch and the parametric domain $\mathcal{Q}$ of a B-spline surface patch as shown in Fig. 4. To achieve this goal, we first introduce the definition of convex combination mapping and Theorem 4.1 from [30].

Definition 3 ([30]). Consider a mapping $\sigma_V : V \to \mathbb{R}^2$ that transforms the vertices $\mathbf{v} \in V$ of a triangulation $\mathcal{T}$ into points in $\mathbb{R}^2$. The mapping σ_V is termed a convex combination mapping if, for every interior vertex $\mathbf{v}$, its image $\sigma_V(\mathbf{v})$ is a convex combination of the images of its neighboring vertices. That is

$$\sigma_V(\mathbf{v}) = \sum_{\mathbf{w} \in \mathcal{N}_{\mathbf{v}}} \lambda_{\mathbf{v}\mathbf{w}} \sigma_V(\mathbf{w}) \tag{8}$$

where $\mathcal{N}_{\mathbf{v}}$ denotes the set of neighbors of $\mathbf{v}$, and all the weights $\lambda_{\mathbf{v}\mathbf{w}}$ are positive and satisfy

$$\sum_{\mathbf{w} \in \mathcal{N}_{\mathbf{v}}} \lambda_{\mathbf{v}\mathbf{w}} = 1.$$

Theorem 1 ([30]). *Suppose $\mathcal{T}$ is a strongly connected triangulation and that $\sigma_V : V \to \mathbb{R}^2$ is a convex combination mapping which maps $\partial D_{\mathcal{T}}$ homeomorphically into the boundary $\partial \mathcal{Q}$ of some (closed) convex region $\mathcal{Q} \subset \mathbb{R}^2$. Then σ_V is one-to-one.*

Várady et al. devised a local parameterization scheme for the Generalized Bézier surface, as detailed in their study [31]. Building on this foundation, we define the mapping function σ in the ensuing discussion.

Theorem 2. *Let λ_i $(i = 1, 2, \ldots, N)$ represent the Wachspress barycentric coordinates of an N-sided convex polygonal domain $\mathcal{P}$, and let $\mathcal{Q}$ denote a unit square. Then, for all $i = 1, 2, \ldots, N$, the mapping $\sigma : \mathcal{P} \to \mathcal{Q}$*

$$\begin{cases} \xi_i = \dfrac{\lambda_i(u, v)}{\lambda_{i-1}(u, v) + \lambda_i(u, v)}, \\ \eta_i = 1 - \lambda_{i-1}(u, v) - \lambda_i(u, v), \end{cases} \tag{9}$$

is bijective. Here, we set $\lambda_0 = \lambda_N$.

Proof. As observed from the properties of Wachspress barycentric coordinates, ξ_i ranges from 0 to 1 on side Γ_i, with η_i equaling 0. η_i increases linearly from 0 to 1 on sides Γ_{i-1} and Γ_{i+1}, while the corresponding values of ξ_i are 0 and 1, respectively. Moreover, for points on edges Γ_j not immediately adjacent to Γ_i (specifically, where $j \notin \{i-1, i, i+1\}$), η_i equals 1. It ensures that the mapping σ systematically places vertices $\mathbf{v}_i$ of $\mathcal{P}$ onto the boundary of the quadrilateral domain $\mathcal{Q}$, preserving their ordering.

Without loss of generality, consider the triangulation $\mathcal{T}(V_0)$ of $\mathcal{Q}$ as shown in Fig. 4, where $V_0 = \{\sigma(\mathbf{v}_1), \ldots, \sigma(\mathbf{v}_N)\}$. Let $\mathbf{u}_k = (u, v)^{\mathrm{T}} \in \mathcal{P}$ and $\xi_k = (\xi_i^k, \eta_i^k)^{\mathrm{T}} = \sigma(\mathbf{u}_k) = \sigma_{V_1}(\mathbf{u}_k) \in \mathcal{Q}$, and $k = 1, 2$. We construct a triangulation for $V_1 = \{\sigma(\mathbf{v}_1), \ldots, \sigma(\mathbf{v}_N), \xi_1, \xi_2\}$ such that $\sigma_{V_1} = \sigma|_{V_1}$ is a convex combination mapping on $\mathcal{T}(V_1)$. The positions of ξ_1 and ξ_2 can be categorized into the following cases:

(1) Fig. 5(a): Both ξ_1 and ξ_2 on the boundaries of triangular elements. In this case, both ξ_1 and ξ_2 can be expressed as convex combinations of their two adjacent vertices.
(2) Fig. 5(b): One on the boundary and one inside a triangular element. Suppose ξ_1 is on the boundary and ξ_2 is inside a triangular element. Connecting ξ_2 to the vertices of its element allows both ξ_1 and ξ_2 to be represented using linear or triangular coordinates.
(3) Fig. 5(c): Different triangular elements. If ξ_1 and ξ_2 are in different triangular elements, connect them to the vertices of their respective elements. They can then be expressed using triangular barycentric coordinates in (8).
(4) Fig. 5(d): Same boundary triangle. If ξ_1 and ξ_2 are within the same boundary triangle, divide them into two new triangles using a line through a vertex. This facilitates their representation using (8).
(5) Fig. 5(e): Same interior triangle and collinear case. If ξ_1 and ξ_2 are in the same interior triangle and collinear with $\sigma(\mathbf{v}_{i-1})$, they can be represented using linear or triangular coordinates.
(6) Fig. 5(f): Same interior triangle and non-collinear case. If ξ_1 and ξ_2 are within the same interior triangle but not collinear
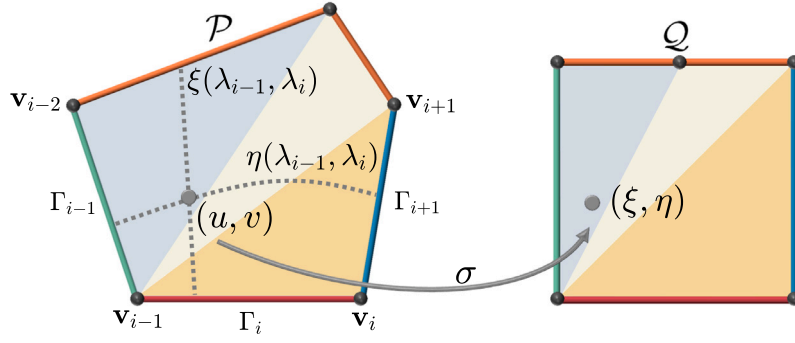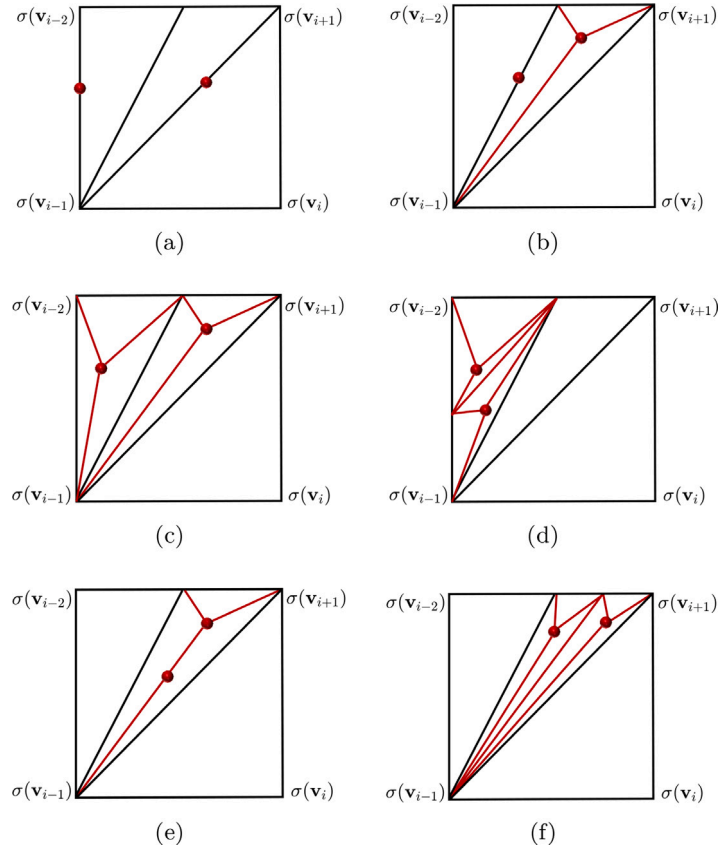
Fig. 4. Schematic illustration of the bijective mapping σ.

Fig. 5. All possible triangulations in the proof of Theorem 2.

with $\sigma(\mathbf{v}_{i-1})$, divide them into two new triangles using a line through $\sigma(\mathbf{v}_{i-1})$. They can be represented using (8) with two new triangles.

All the possible triangulations mentioned above satisfy Theorem 1, ensuring that σ_{V_1} is one-to-one. Therefore, if $\xi_1 \neq \xi_2$, then $\boldsymbol{u}_1 \neq \boldsymbol{u}_2$ proving that σ is injective.

For surjectivity, consider that the continuity of the Wachspress coordinates ensures that ξ_i spans the interval $[0, 1]$ across the side Γ_i, with η_i ranging from 0 to 1 along its adjoining sides Γ_{i-1} and Γ_{i+1}. The continuity of σ implies its surjectivity. $\quad\square$

Remark 1. According to Theorem 2, for each vertex $\mathbf{v}_i, i = 1, 2, \dots, N$, there exists a corresponding mapping σ. As Fig. 4 shows, under the action of mapping σ, sides $\Gamma_{i-1}, \Gamma_i, \Gamma_{i+1}$ of $\mathcal{P}$ are mapped to 3 sides of $\mathcal{Q}$, respectively, while the remaining sides of $\mathcal{P}$ are mapped to the other side of $\mathcal{Q}$ (marked with orange lines). It is necessary to flexibly choose the appropriate mapping for different problems.

3.2. Parameterization quality improvement of composite toric parameterization

Given a lattice points set $\mathcal{A}$, control points $\mathbf{P}$ and weights $\boldsymbol{\omega}$, the polygonal domain Ω is parameterized by (1), e.g.

$$(x, y) = S(u, v), \forall (u, v) \in \Delta_{\mathcal{A}}, \tag{10}$$

and S refers to the parameterization of Ω. For isotropic parameterizations that are independent of the governing equations, based on injectivity, optimal uniformity and orthogonality are required. However, in MS-GIFT, the parametric domain of the geometry differs from that of the solution. As a result, it is more practical to optimize the composite toric parameterization $S \circ \sigma^{-1}$.

Similar to the method in [32], we utilize a three-step parameterization approach to construct an analysis-suitable composite toric parameterization, effectively addressing the aforementioned issue.
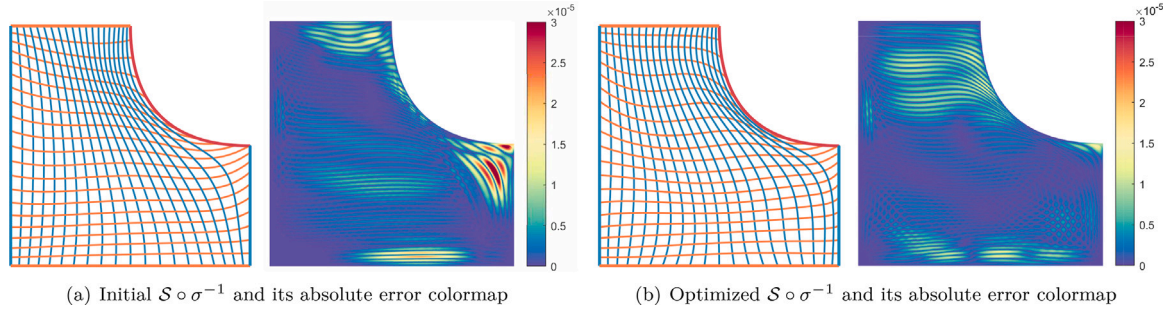
(a) Initial $\mathcal{S} \circ \sigma^{-1}$ and its absolute error colormap   (b) Optimized $\mathcal{S} \circ \sigma^{-1}$ and its absolute error colormap

Fig. 6. Different composite toric parameterizations $\mathcal{S} \circ \sigma^{-1}$ may affect the absolute error in MS-GIFT. (For interpretation of the references to color in this figure legend, the reader is referred to the web version of this article.)

(1) **Initialization.** Given a set of lattice points, boundary control points and weights. For each inner lattice point, connect the boundary control points corresponding to the boundary lattice points of the same column and row, the intersection of the resulting two lines is set as an inner control point. The inner weight is taken as the product of the boundary weights whose lattice points are located in the same column or row as the corresponding inner lattice point.

(2) **Foldover Elimination.** Let $\mathcal{J}_{\mathcal{S} \circ \sigma^{-1}}$ represent the Jacobian of the composite toric parameterization $\mathcal{S} \circ \sigma^{-1}$. The foldovers can then be eliminated by solving the subsequent optimization problem:

$$\underset{\mathbf{P_a}, \mathbf{a} \in \text{inner}(\mathcal{A})}{\arg\min} \int_{\mathcal{Q}} \max\{0, \delta - |\mathcal{J}_{\mathcal{S} \circ \sigma^{-1}}|\} \mathrm{d}\mathcal{Q}, \tag{11}$$

where δ is a user-specified parameter. We set δ to $0.05 * \text{area}(\Omega)$ in our experiments.

(3) **Parameterization quality improvement.** For further enhancement of the resulting parameterization quality, we take into account both the corrected Winslow energy functional

$$\mathcal{E}^{\mathrm{CW}}(\mathbf{P_a}; \omega_{\mathbf{a}}) = \int_{\mathcal{Q}} \frac{\mathrm{trace}\left(\mathcal{J}_{\mathcal{S} \circ \sigma^{-1}}^{\mathrm{T}} \mathcal{J}_{\mathcal{S} \circ \sigma^{-1}}\right)}{\max\{0, |\mathcal{J}_{\mathcal{S} \circ \sigma^{-1}}|\} + \varepsilon} \, \mathrm{d}\mathcal{Q}, \tag{12}$$

and the uniformity energy functional

$$\mathcal{E}^{\mathrm{Unif.}}(\mathbf{P_a}; \omega_{\mathbf{a}}) = \int_{\mathcal{Q}} \left(\frac{|\mathcal{J}_{\mathcal{S} \circ \sigma^{-1}}|}{\text{area}(\Omega)} - 1\right)^2 \mathrm{d}\mathcal{Q}, \tag{13}$$

where ε is a small positive threshold to prevent division by zero. Subsequently, we solve the following two unconstrained optimization problems alternately:

$$\underset{\mathbf{P_a}, \mathbf{a} \in \text{inner}(\mathcal{A})}{\arg\min} \quad \mathcal{E}^{\mathrm{CW}}(\mathbf{P_a}, \omega_{\mathbf{a}}) + \lambda \mathcal{E}^{\mathrm{Unif.}}, \tag{14}$$

and

$$\underset{\omega_{\mathbf{a}}, \mathbf{a} \in \text{inner}(\mathcal{A})}{\arg\min} \quad \mathcal{E}^{\mathrm{CW}}(\mathbf{P_a}, \omega_{\mathbf{a}}) + \lambda \mathcal{E}^{\mathrm{Unif.}}, \tag{15}$$

with a positive parameter λ for equilibrium between $\mathcal{E}^{\mathrm{CW}}$ and $\mathcal{E}^{\mathrm{Unif.}}$.

Fig. 6(a) displays an initial composite toric parameterization, constructed by keeping control points identical to the lattice points, except for the bevel edge, which is adjusted to recover the circular arc. Noticeably, some non-uniform elements emerge near the upper-right corner. A Poisson problem with homogeneous boundary conditions, solved using this initial parameterization, yields a large absolute error in the affected region, as depicted on the right. The parameterization optimized through the aforementioned three-step approach, illustrated in Fig. 6(b), shows amelioration of the non-uniform elements. The corresponding absolute error colormap on the right indicates that the optimized composite toric parameterization $\mathcal{S} \circ \sigma^{-1}$ effectively reduces the numerical error.

4. Formalism for Multi-sided Geometry-Independent Field approximaTion (MS-GIFT)

In this section, we demonstrate our proposed MS-GIFT method for solving Poisson's equation and linear elasticity problem. The gradients of the shape functions, which are essential for the subsequent analysis, are calculated in Section 4.1. Subsequently, the weak forms and error estimates for these two problems are deduced in Sections 4.2 and 4.3, respectively. Based on these, we formulate Algorithm 1, which summarizes the overall workflow.

4.1. Gradient computation for shape functions

Upon obtaining the multi-sided composite toric parameterization, we next compute the gradient formulations of the shape function $N_p \circ \sigma \circ \mathcal{S}^{-1}$. To simplify the notations, let $\boldsymbol{u} = (u, v)^{\mathrm{T}} \in \mathcal{P}$, $\boldsymbol{\xi} = (\xi, \eta)^{\mathrm{T}} \in \mathcal{Q}$, and $\boldsymbol{x} = (x, y)^{\mathrm{T}} \in \Omega$ denote the parameters for toric surface patches, the parameters for B-splines or THB-splines, and the physical coordinates, respectively.

Based on the gradient formula of Wachspress barycentric coordinates (7) and the chain rule, we obtain

$$\nabla_{\boldsymbol{u}} \xi = \frac{\lambda_{i-1} \nabla_{\boldsymbol{u}} \lambda_i - \lambda_i \nabla_{\boldsymbol{u}} \lambda_{i-1}}{(\lambda_{i-1} + \lambda_i)^2},$$
$$\nabla_{\boldsymbol{u}} \eta = -\nabla_{\boldsymbol{u}} \lambda_{i-1} - \nabla_{\boldsymbol{u}} \lambda_i, \tag{16}$$

then yields the Jacobian matrix $\mathcal{J}_{\sigma}$ of the one-to-one mapping σ

$$\mathcal{J}_{\sigma} = (\nabla_{\boldsymbol{u}} \xi, \nabla_{\boldsymbol{u}} \eta)^{\mathrm{T}}. \tag{17}$$

The Jacobian matrix $\mathcal{J}_S$ of the toric parameterization S can be computed by

$$\mathcal{J}_S = \begin{pmatrix} \frac{\partial x}{\partial u} & \frac{\partial x}{\partial v} \\ \frac{\partial y}{\partial u} & \frac{\partial y}{\partial v} \end{pmatrix}$$
$$= \frac{1}{\left(\sum_{\mathbf{a} \in \mathcal{A}} \omega_{\mathbf{a}} \beta_{\mathbf{a}}\right)^2} \left(\left(\sum_{\mathbf{a} \in \mathcal{A}} \omega_{\mathbf{a}} \mathbf{P_a} \nabla_{\boldsymbol{u}}^{\mathrm{T}} \beta_{\mathbf{a}}\right) \left(\sum_{\mathbf{a} \in \mathcal{A}} \omega_{\mathbf{a}} \beta_{\mathbf{a}}\right) - \right. \tag{18}$$
$$\left. \left(\sum_{\mathbf{a} \in \mathcal{A}} \omega_{\mathbf{a}} \mathbf{P_a} \beta_{\mathbf{a}}\right) \left(\sum_{\mathbf{a} \in \mathcal{A}} \omega_{\mathbf{a}} \nabla_{\boldsymbol{u}}^{\mathrm{T}} \beta_{\mathbf{a}}\right)\right).$$

Therefore, the Jacobian matrix of the inverse mapping $\sigma \circ S^{-1}$ for the composite toric parameterization can be calculated using the following formulas:

$$\mathcal{J}_{\sigma \circ S^{-1}} = \begin{pmatrix} \frac{\partial \xi}{\partial x} & \frac{\partial \xi}{\partial y} \\ \frac{\partial \eta}{\partial x} & \frac{\partial \eta}{\partial y} \end{pmatrix}$$
$$= \begin{pmatrix} \frac{\partial \xi}{\partial u} & \frac{\partial \xi}{\partial v} \\ \frac{\partial \eta}{\partial u} & \frac{\partial \eta}{\partial v} \end{pmatrix} \begin{pmatrix} \frac{\partial u}{\partial x} & \frac{\partial u}{\partial y} \\ \frac{\partial v}{\partial x} & \frac{\partial v}{\partial y} \end{pmatrix} = \mathcal{J}_{\sigma} \mathcal{J}_S^{-1}. \tag{19}$$

Applying the chain rule of derivatives, again, the gradients of the shape function $N_p \circ \sigma \circ S^{-1}$ concerning the physical coordinates $\boldsymbol{x}$ can

be determined as follows:

$$
\nabla_x N_p = \begin{pmatrix} \frac{\partial N_p}{\partial x} \\ \frac{\partial N_p}{\partial y} \end{pmatrix} = \begin{pmatrix} \frac{\partial \xi}{\partial x} & \frac{\partial \eta}{\partial x} \\ \frac{\partial \xi}{\partial y} & \frac{\partial \eta}{\partial y} \end{pmatrix} \begin{pmatrix} \frac{\partial N_p}{\partial \xi} \\ \frac{\partial N_p}{\partial \eta} \end{pmatrix} \tag{20}
$$
$$
= (\boldsymbol{J}_{\sigma \circ S^{-1}})^{\mathrm{T}} \nabla_\xi N_p.
$$

4.2. Poisson's equation

As an illustration, we consider Poisson's equation with homogeneous Dirichlet boundary conditions

$$
\begin{aligned}
-\nabla^2 \mathcal{U}(\boldsymbol{x}) &= f(\boldsymbol{x}), \quad \boldsymbol{x} \in \Omega \\
\mathcal{U}(\boldsymbol{x}) &= 0, \quad \boldsymbol{x} \in \partial\Omega,
\end{aligned} \tag{21}
$$

where $\mathcal{U}(\boldsymbol{x})$ is the unknown solution, f is a given source term, and $\partial\Omega$ is the boundary of the computational domain Ω.

Following the principle of GIFT, the solution can be expressed as a linear combination of B-spline or THB-spline basis functions (collectively denoted as N_q) using MS-GIFT method in this paper:

$$
\mathcal{U}^{\mathrm{h}} = \sum_{q=1}^{\mathrm{ndofs}} \mathcal{U}_q N_q(\boldsymbol{\xi}), \tag{22}
$$

where $\mathcal{U}_q$ are the unknown control variable, ndofs is the number of degrees-of-freedom (DOFs).

The weak form for the above Poisson's Eq. (21) is given by

$$
a(\mathcal{U}, \mathcal{V}) = \int_\Omega \nabla\mathcal{U}\nabla\mathcal{V}\,\mathrm{d}\Omega, \quad \ell(\mathcal{V}) = \int_\Omega f\mathcal{V}\,\mathrm{d}\Omega. \tag{23}
$$

By substituting the toric geometry (10) and the (TH)B-spline solution (22) into the weak form (23), we obtain

$$
a\left(\sum_{q=1}^{\mathrm{ndofs}} \mathcal{U}_q N_q(\boldsymbol{x}), N_p(\boldsymbol{x})\right) = \sum_{q=1}^{\mathrm{ndofs}} \mathcal{U}_q a(N_q(\boldsymbol{x}), N_p(\boldsymbol{x})),
$$
$$
\ell(N_p(\boldsymbol{x})) = \int_\Omega f(\boldsymbol{x}) N_p(\boldsymbol{x})\mathrm{d}\Omega
$$

where $p = 1, 2, \ldots, \mathrm{ndofs}$.

Denote

$$
\begin{aligned}
\mathbf{K}_{p,q} &= a(N_q(\boldsymbol{x}), N_p(\boldsymbol{x})) \\
&= \int_\Omega \nabla_x N_q(\boldsymbol{x}) \nabla_x N_p(\boldsymbol{x})\mathrm{d}\Omega, \\
\mathbf{f}_p &= \ell(N_p(\boldsymbol{x})) = \int_\Omega f(\boldsymbol{x}) N_p(\boldsymbol{x})\mathrm{d}\Omega
\end{aligned} \tag{24}
$$

to reveal the following linear system

$$
\sum_{q=1}^{\mathrm{ndofs}} \mathbf{K}_{p,q} \mathcal{U}_q = \mathbf{f}_p, \quad p = 1, 2, \ldots, \mathrm{ndofs}
$$

whose matrix form is

$$
\mathbf{K}(\mathcal{U}_q) = \mathbf{f}, \quad (\mathcal{U}_q) \in \mathbb{R}^{\mathrm{ndofs}}. \tag{25}
$$

The stiffness matrix $\mathbf{K}$ and the force vector $\mathbf{f}$ are defined by (24).

The error between the exact solution $\mathcal{U}^{\mathrm{exact}}$ and the numerical solution $\mathcal{U}^{\mathrm{h}}$ is measured by the following relative L_2 error

$$
e = \sqrt{\frac{\int_\Omega (\mathcal{U}^{\mathrm{exact}} - \mathcal{U}^{\mathrm{h}})^2\,\mathrm{d}\Omega}{\int_\Omega (\mathcal{U}^{\mathrm{exact}})^2\,\mathrm{d}\Omega}}. \tag{26}
$$

4.3. Linear elasticity problem

To demonstrate the robustness of the proposed method, we consider a more complex linear elasticity problem which takes into account displacements in two directions, denoted by $\boldsymbol{\mathcal{U}} := (\mathcal{U}_1, \mathcal{U}_2)^{\mathrm{T}}$.

Given Young's modulus E and Poisson's coefficient ν, stresses can be represented by

$$
\boldsymbol{\sigma} = \begin{pmatrix} \sigma_x \\ \sigma_y \\ \tau_{xy} \end{pmatrix} = \mathbf{D}\boldsymbol{\varepsilon} = \begin{pmatrix} \frac{E}{1-\nu^2} & \frac{\nu E}{1-\nu^2} & 0 \\ \frac{\nu E}{1-\nu^2} & \frac{E}{1-\nu^2} & 0 \\ 0 & 0 & \frac{E}{2(1+\nu)} \end{pmatrix} \begin{pmatrix} \varepsilon_x \\ \varepsilon_y \\ \gamma_{xy} \end{pmatrix},
$$

where strains $\boldsymbol{\varepsilon}$ are defined by

$$
\boldsymbol{\varepsilon} = \begin{pmatrix} \varepsilon_x \\ \varepsilon_y \\ \gamma_{xy} \end{pmatrix} = \begin{pmatrix} \frac{\partial}{\partial x} & 0 \\ 0 & \frac{\partial}{\partial y} \\ \frac{\partial}{\partial y} & \frac{\partial}{\partial x} \end{pmatrix} \begin{pmatrix} \mathcal{U}_1 \\ \mathcal{U}_2 \end{pmatrix}.
$$

Analogously, the numerical solution of displacements is written as

$$
\mathcal{U}_1^{\mathrm{h}} = \sum_{q=1}^n \mathcal{U}_{1,q} N_q(\boldsymbol{\xi}), \quad \mathcal{U}_2^{\mathrm{h}} = \sum_{q=1}^n \mathcal{U}_{2,q} N_q(\boldsymbol{\xi})
$$

which also yields a matrix notation

$$
\boldsymbol{\mathcal{U}}^h = \begin{pmatrix} N_1 & 0 & N_2 & 0 & \ldots & N_n & 0 \\ 0 & N_1 & 0 & N_2 & \ldots & 0 & N_n \end{pmatrix} \begin{pmatrix} \mathcal{U}_{1,1} \\ \mathcal{U}_{2,1} \\ \mathcal{U}_{1,2} \\ \mathcal{U}_{2,2} \\ \vdots \\ \mathcal{U}_{1,n} \\ \mathcal{U}_{2,n} \end{pmatrix} \tag{27}
$$

with ndofs $= 2n$.

The weak form of the linear elasticity problem is given by

$$
\begin{aligned}
a(\boldsymbol{\mathcal{U}}, \boldsymbol{\mathcal{V}}) &= \int_\Omega \boldsymbol{\varepsilon}(\boldsymbol{\mathcal{U}})^{\mathrm{T}} \mathbf{D}\boldsymbol{\varepsilon}(\boldsymbol{\mathcal{V}})\mathrm{d}\Omega, \\
\ell(\boldsymbol{\mathcal{V}}) &= \int_\Omega f\boldsymbol{\mathcal{V}}\,\mathrm{d}\Omega + \int_{\partial\Omega_N} \tilde{t}\boldsymbol{\mathcal{V}}\,\mathrm{d}\Gamma,
\end{aligned} \tag{28}
$$

where f is the given body forces, $\tilde{t}$ is the given traction prescribed on $\partial\Omega_N$. Substituting the toric geometry (10) and the (TH)B-spline solution (27) into (28), we obtain

$$
a(\boldsymbol{\mathcal{U}}^h, N_p(\boldsymbol{x})) = \int_\Omega \boldsymbol{\varepsilon}(\boldsymbol{\mathcal{U}}^h)^{\mathrm{T}} \mathbf{D}\boldsymbol{\varepsilon}(N_p(\boldsymbol{x}))\mathrm{d}\Omega
$$
$$
= \sum_{q=1}^n \begin{pmatrix} \mathcal{U}_{1,q} \\ \mathcal{U}_{2,q} \end{pmatrix}^{\mathrm{T}} \int_\Omega \begin{pmatrix} \frac{\partial N_q}{\partial x} & 0 & \frac{\partial N_q}{\partial y} \\ 0 & \frac{\partial N_q}{\partial y} & \frac{\partial N_q}{\partial x} \end{pmatrix} \mathbf{D} \begin{pmatrix} \frac{\partial N_p}{\partial x} & 0 \\ 0 & \frac{\partial N_p}{\partial y} \\ \frac{\partial N_p}{\partial y} & \frac{\partial N_p}{\partial x} \end{pmatrix} \mathrm{d}\Omega
$$
$$
= \sum_{q=1}^n \begin{pmatrix} \mathcal{U}_{1,q} \\ \mathcal{U}_{2,q} \end{pmatrix}^{\mathrm{T}} \int_\Omega \boldsymbol{B}_q^{\mathrm{T}} \mathbf{D} \boldsymbol{B}_p \mathrm{d}\Omega
$$

and

$$
\ell(N_p(\boldsymbol{x})) = \int_\Omega f(\boldsymbol{x}) N_p(\boldsymbol{x})\mathrm{d}\Omega + \int_{\partial\Omega_N} \tilde{t}(\boldsymbol{x}) N_p(\boldsymbol{x})\mathrm{d}\Gamma.
$$

Thus, the components of the stiffness matrix and force vector are denoted as

$$
\mathbf{K}_{p,q} = \int_\Omega \boldsymbol{B}_q^{\mathrm{T}} \mathbf{D} \boldsymbol{B}_p \mathrm{d}\Omega, \quad \mathbf{f}_p = \ell(N_p(\boldsymbol{x})) \tag{29}
$$

which form the following linear system

$$
\sum_q^n \mathbf{K}_{p,q} \begin{pmatrix} \mathcal{U}_{1,q} \\ \mathcal{U}_{2,q} \end{pmatrix} = \mathbf{f}_p, \quad p = 1, 2, \ldots, n, \tag{30}
$$

notice that the sizes of $\mathbf{K}_{p,q}$ and $\mathbf{f}_p$ are 2×2 and 2×1, respectively. The errors are measured by displacement norm error and energy norm

error

$$e_{\text{disp}} = \sqrt{\iint_\Omega (\boldsymbol{\mathscr{U}}^{\text{exact}} - \boldsymbol{\mathscr{U}}^{\text{h}})^{\text{T}}(\boldsymbol{\mathscr{U}}^{\text{exact}} - \boldsymbol{\mathscr{U}}^{\text{h}}) \, d\Omega},$$

$$e_{\text{energy}} = \sqrt{\iint_\Omega (\boldsymbol{\varepsilon}^{\text{exact}} - \boldsymbol{\varepsilon}^{\text{h}})^{\text{T}}(\boldsymbol{\sigma}^{\text{exact}} - \boldsymbol{\sigma}^{\text{h}}) \, d\Omega},$$

(31)

where $\boldsymbol{\mathscr{U}}^{\text{exact}}$, $\boldsymbol{\sigma}^{\text{exact}}$ and $\boldsymbol{\varepsilon}^{\text{exact}}$ are the exact displacement, stress, and strain, and $\boldsymbol{\mathscr{U}}^{\text{h}}$, $\boldsymbol{\sigma}^h$, and ε^{h} denote the numerical displacement, stress, and strain, respectively.

4.4. Overview of multi-sided geometry-Independent Field approximaTion approach

In summary, we obtain an algorithm for isogeometric analysis using MS-GIFT as described in Algorithm 1.

Algorithm 1: MS-GIFT: Multi-Sided Geometry-Independent Field approximaTion approach for isogeometric analysis

Input: U: quadrature points set;
　　　　// Toric geometry
　　　$\mathcal{A}$: lattice points set;　　**P**: control points set;
　　　$\boldsymbol{\omega}$: weights set;
　　　// B-spline basis
　　　Ξ, $\mathcal{H}$: knot vectors;　　p, q: degrees.
Output: $\mathscr{U}^h$: IGA solution.

1　Get $n = \#(\mathcal{A})$; // Number of toric control points

　// Calculate parameter transformation
　　　symbolically
2　Compute the one-to-one mapping σ between parametric domains;
3　Compute its inverse mapping σ^{-1};
4　Compute $\mathcal{J}_\sigma$ in (17);

　// Calculate gradient information of toric
　　　parameterization
5　**for** $u \in U$ **do**
6　　　Compute toric basis functions and their derivatives at u;
7　　　Compute $\mathcal{J}_S$ at u according to (18);

　　　// Form the linear system and solve
8　　　Compute B-spline basis functions and their derivatives at u;
9　　　Compute points $x = S(u)$ of the computational domain;
10　　Compute $\nabla_x N_k$ at u according to (20);
11　**end**
12　Compute $\mathbf{K}_{p,q}$ and $\mathbf{f}_p$ in (24) or (29);
13　Assemble the stiffness matrix $\mathbf{K}$ and the force vector $\mathbf{f}$;
14　Impose Dirichlet boundary conditions;
15　Solving the linear system (25) or (30) to obtain the IGA solution $\mathscr{U}^h$.
16　**return** $\mathscr{U}^h$

Remark 2. In contrast to general refinement methods employed to increase DOFs in IGA, MS-GIFT simply requires the input of refined knot vectors and degrees for each step to refine.

4.5. Adaptive refinement by using THB-splines

Algorithm 1 outlines the process of employing B-spline basis for analysis. Fundamentally, the classical refinement strategies of B-spline basis suffer from a lack of locality, as each step propagates over a large element, resulting in a high number of redundant DOFs. To address this issue, THB-spline has been employed, as it enables efficient local refinement. Furthermore, THB-spline allows for the allocation of more

DOFs in areas where the numerical solution error is significant, thereby significantly reducing the error.

The numerical solutions approximated by THB splines are based on the following adaptive loop [33]:

(1) **Solve.** Solve the Poisson's Eq. (21) through MS-GIFT method with the current THB-spline basis. Denote the solution as $\mathscr{U}^h$.
(2) **Estimate.** We employ the element-based error indicator [33]

$$\varepsilon_Q = diam(S \circ \sigma^{-1}(Q)) \left(\int_{S \circ \sigma^{-1}(Q)} |f + \Delta \mathscr{U}^h|^2 \right)^{\frac{1}{2}}$$

(32)

for each active element Q in parametric domain $\mathcal{Q}$ and the corresponding active element $S \circ \sigma^{-1}(Q)$ in computational domain Ω.

(3) **Mark.** Find the active elements Q_M that satisfies

$$\varepsilon_{Q_M} \ge \theta \max \varepsilon_Q,$$

(33)

where $\theta = 0.5$.

(4) **Refine.** Refine the marked elements Q_M and repeat the process above until the error (26) is less than a given tolerance.

5. Numerical experiments

To showcase the efficacy and superiority of our proposed MS-GIFT method, a comparison with traditional IGA method is available in this section. The importance of improving the composite toric parameterization quality is effectively illustrated by the error history plots provided for each example. These plots clearly differentiate the outcomes achieved with the initial toric parameterization, referred to as MS-GIFT (initial), from those obtained after optimization, denoted as MS-GIFT (optimal).

Specifically, in Section 5.1, we juxtapose MS-GIFT against NURBS h-refinement and toric p-refinement methods. Additionally, in Section 5.2, MS-GIFT is also compared with the adaptive THB method. In order to ensure fairness, we maintain consistency in the degrees and refinement strategy of shape functions employed in MS-GIFT, NURBS, and THB methods. The degree specifics of the spline configurations employed for analysis in each example have been listed in Appendix B.

Furthermore, we present two methodologies for determining the inverse mapping σ^{-1} between the $N-$sided polygon and unit square. In instances where $N < 7$, we adopted the MATLAB Symbolic Math Toolbox to solve σ inversely. Conversely, for scenarios with $N \ge 7$, σ^{-1} is obtained by solving the following optimization problem:

$$\arg\min_{(u,v)} \quad \|(\xi_i, \eta_i) - \sigma(u,v)\|,$$
$$\text{s.t.} \quad\quad L_i(u,v) \ge 0.$$

(34)

In our experiments, the choice of the mapping σ is selected by the following two considerations:

(1) **Boundary conditions.** In scenarios with distinct boundary conditions on each boundary, such as Dirichlet and Neumann boundary conditions, our approach avoids conflating boundaries with differing boundary conditions onto a single side of the quadrilateral domain $\mathcal{Q}$;
(2) **Mapping simplicity.** For the polygon vertex with an internal angle of 90 degrees, the inverse mapping associated with σ is notably simpler. We thus recommend this mapping form to avoid additional computational complexity, ensuring efficiency without sacrificing computational accuracy.

Furthermore, a reference implementation is currently under development utilizing the open-source C++ library, Geometry + Simulation Modules [34,35].
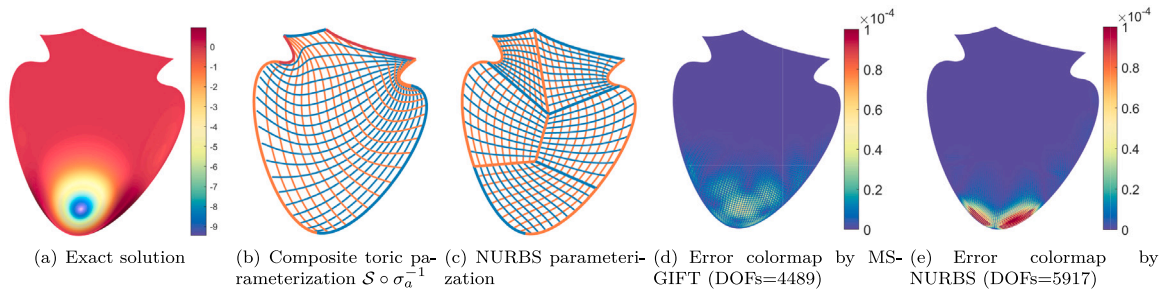
(a) Exact solution   (b) Composite toric parameterization $\mathcal{S} \circ \sigma_a^{-1}$ (c) NURBS parameterization   (d) Error colormap by MS-GIFT (DOFs=4489)   (e) Error colormap by NURBS (DOFs=5917)

Fig. 7. Strawberry: a hexagonal computational domain. (For interpretation of the references to color in this figure legend, the reader is referred to the web version of this article.)
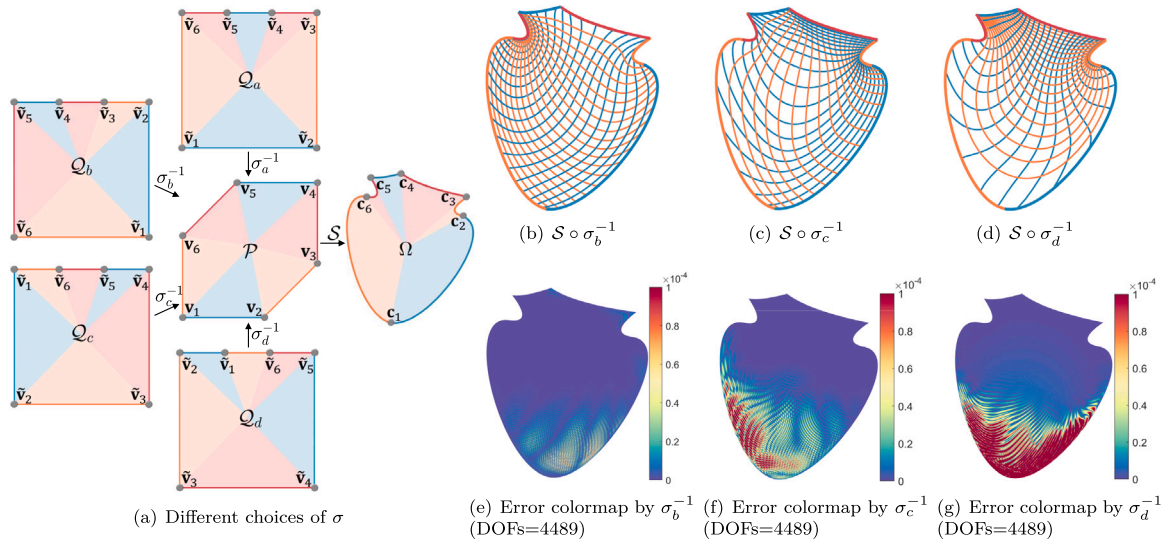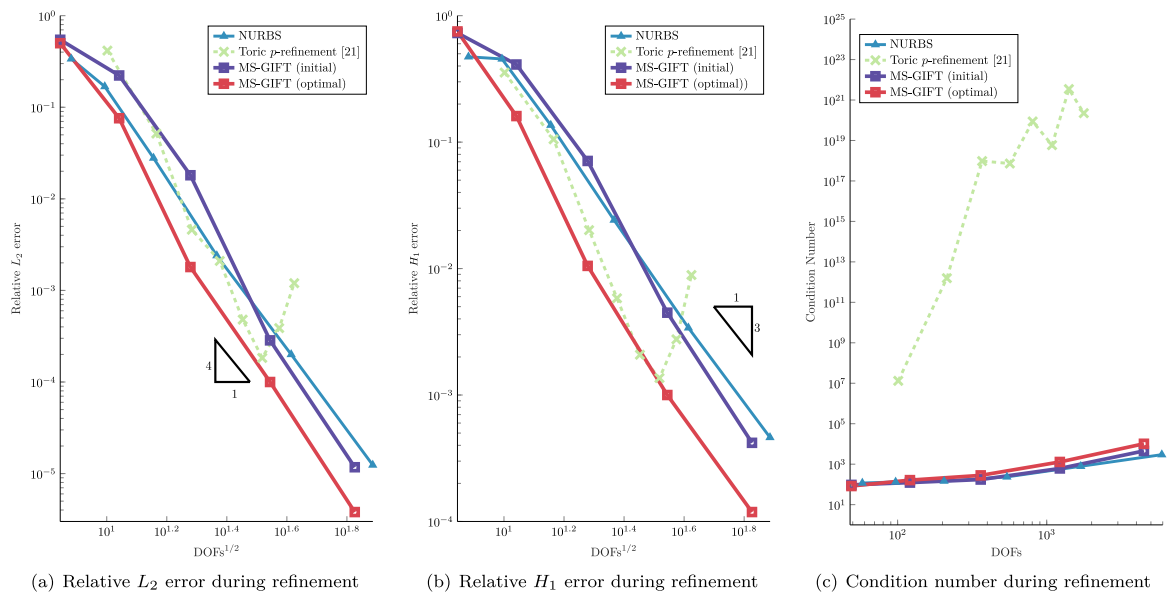

(a) Different choices of σ

(b) $\mathcal{S} \circ \sigma_b^{-1}$ (c) $\mathcal{S} \circ \sigma_c^{-1}$ (d) $\mathcal{S} \circ \sigma_d^{-1}$

(e) Error colormap by σ_b^{-1} (DOFs=4489)   (f) Error colormap by σ_c^{-1} (DOFs=4489)   (g) Error colormap by σ_d^{-1} (DOFs=4489)

Fig. 8. Different choices of σ and their corresponding error colormaps.. (For interpretation of the references to color in this figure legend, the reader is referred to the web version of this article.)

(a) Relative L_2 error during refinement   (b) Relative H_1 error during refinement   (c) Condition number during refinement

Fig. 9. Strawberry: convergence curve of error and the condition number of the stiffness matrices during refinement.

(a) Exact solution (b) Composite toric parameterization (c) NURBS parameterization (d) Error colormap by MS-GIFT (DOFs=4356) (e) Error colormap by NURBS (DOFs=4400)
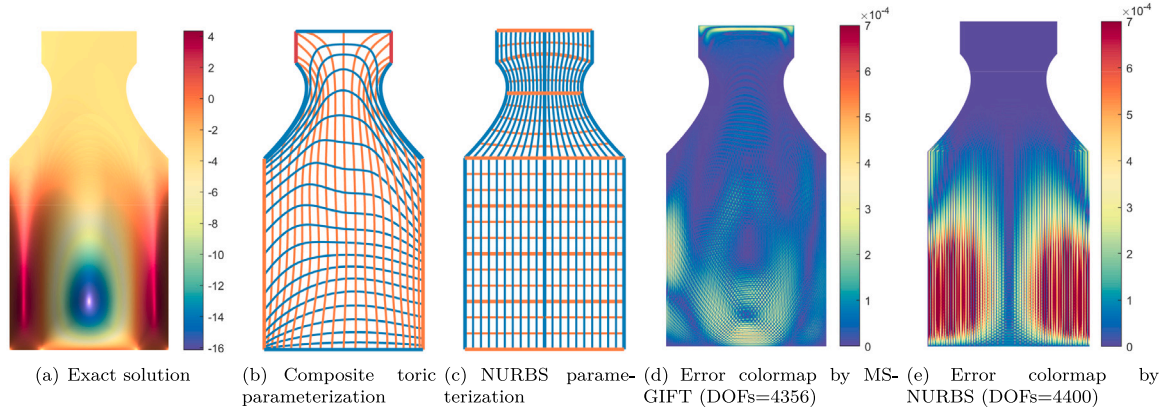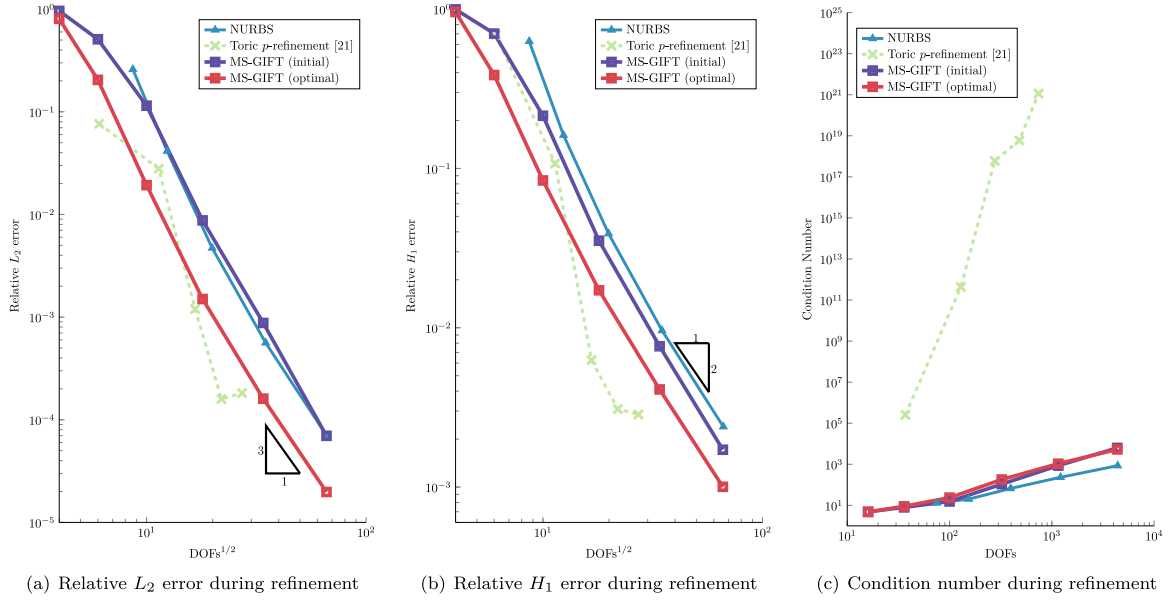
Fig. 10. Bottle: an octagonal computational domain. (For interpretation of the references to color in this figure legend, the reader is referred to the web version of this article.)

(a) Relative L_2 error during refinement (b) Relative H_1 error during refinement (c) Condition number during refinement

Fig. 11. Bottle: convergence curve of error and the condition number of the stiffness matrices during refinement.

5.1. Poisson's equation solved by uniform refinement

Consider Poisson's Eq. (21) defined over a hexagonal computational domain. The exact solution is depicted in Fig. 7(a), whose expression can be found in Appendix A.

The parameterizations represented by a toric surface patch and a NURBS surface are displayed in Fig. 7(b) and Fig. 7(c), respectively. In this example, Fig. 7(b) is constructed using the mapping σ_a, as shown in Fig. 8(a). All subsequent comparisons with other methods are based on this same mapping, σ_a. A distinctive feature of the NURBS parameterization is its division into 5 patches, which only exhibit C^0 continuity along the interfaces. Through the h-refinement process, the absolute error colormaps corresponding to each parameterization are illustrated in Fig. 7(d) and Fig. 7(e), respectively. Thanks to the smooth parameterization, our method achieves superior numerical solution accuracy.

Since the choice of σ affects the quality of the composite parameterization, it directly influences the accuracy of the subsequent analysis. To illustrate the impact of different σ selections, we present the parameterizations and the corresponding error colormaps for various σ mappings in Fig. 8. It can be seen that higher-quality composite parameterizations, with more uniform element size, yield more precise numerical results.

Fig. 9 presents the evolution of errors and condition numbers for stiffness matrices acquired during refinement using the MS-GIFT, NURBS, and toric p-refinement method [21]. While the toric p-refinement method displays smaller errors under some DOFs, the condition number rapidly increases as the degree of test functions rises, resulting in non-converging errors. In contrast, our method exhibits enhanced stability and a condition number for the stiffness matrix comparable to that of the NURBS method.

Next, we present an example with an octagonal parametric domain as shown in Fig. 10. The representation and colormap of the exact solution are shown in appendix and Fig. 10(a), respectively Employing the parameterization technique introduced in Section 3.2, the resulting composite toric and NURBS parameterization are displayed in Fig. 10(b) and Fig. 10(c), respectively. To ensure a fair comparison and achieve a more uniform element size across the computational domain, the NURBS parameterization has been segmented into 14 patches, as depicted in Fig. 10(c).

After six levels of h-refinement, the absolute error colormaps are displayed in Figs. 10(d)–10(e). It is evident that the proposed method achieves comparable performance while utilizing only two-thirds of the DOFs employed by the NURBS method. Fig. 11 illustrates the evolution of error and condition number of the stiffness matrix solved by the three methods. As the degree of the solution bases is consistent with the one used in the NURBS method, a uniform convergence order is obtained
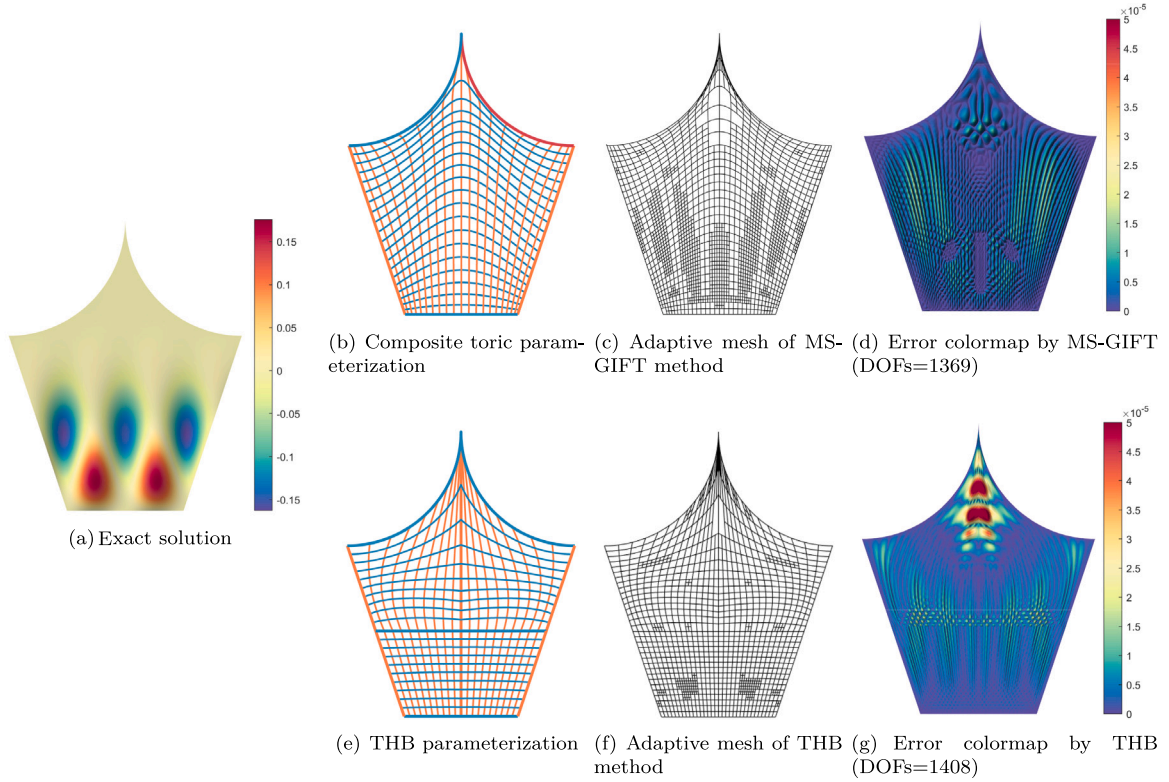
(a) Exact solution

(b) Composite toric parameterization

(c) Adaptive mesh of MS-GIFT method

(d) Error colormap by MS-GIFT (DOFs=1369)

(e) THB parameterization

(f) Adaptive mesh of THB method

(g) Error colormap by THB (DOFs=1408)

Fig. 12. Crown: a pentagonal computational domain.. (For interpretation of the references to color in this figure legend, the reader is referred to the web version of this article.)

following the same h-refinement strategy. The MS-GIFT method is capable of producing numerical solutions with higher continuity and reduced errors.

5.2. Poisson's equation solved by using adaptive refinement

A significant advantage of GIFT is that it simplifies local adaptivity. In this section, we examine MS-GIFT with adaptive refinement strategy in Section 4.5 using THB-splines. The second derivatives involved in (32) are computed numerically in MS-GIFT.

Consider Poisson's Eq. (21) over a pentagonal crown-like computational domain, with the exact solution depicted in Fig. 12(a) and appendix. The initial coarse parameterizations are represented by toric (Fig. 12(b)) and NURBS (Fig. 12(e)) surfaces. Following a series of local refinements guided by function-based error indicators, the adaptive meshes and corresponding absolute error colormaps obtained by MS-GIFT and adaptive isogeometric methods are displayed in the last two columns of Fig. 12. Fig. 14(a) presents the error history of the two adaptive methods. Due to the C^0 continuity within the NURBS parameterization, the resulting error colormap also distinctly reveals the division into two patches in the middle.

Fig. 13 showcases the adaptive meshes and error colormaps of the proposed method at steps 6, 10, and 13. The meshes primarily become denser in areas where the exact solution undergoes significant changes during the refinement process, effectively reducing the error.

Furthermore, we investigate a computational domain shaped as a pentagon, modeling the complex geometry of a female rotor from a twin-screw compressor. The exact solution for this scenario is approximated by a hat function, which diminishes towards the boundaries of the domain and is illustrated in Fig. 15(a). We implement local refinements on a single-patch toric parameterization, as shown in Fig. 15(b), in contrast to the four-patch NURBS parameterization shown in Fig. 15(e). Figs. 15(c) and 15(d) present the respective adaptive meshes derived from these refinements. The convergence behavior

throughout this refinement is displayed in the error history plots of Fig. 14(b).

Although a bijection between arbitrary convex polyhedra and regular hexahedra has not yet been established, the proposed method remains valid for specific 3D computational domains with parametric domains resembling straight prisms, i.e., 2.5-D geometry. As an illustration, we consider Poisson's Eq. (21) over a pentagonal prism, with the exact solution and boundaries depicted in Fig. 16(a). Based on the adaptive meshes provided in Figs. 16(b)–16(c), the absolute error colormaps obtained by the proposed method and the adaptive THB method are displayed in Figs. 16(d)–16(e). Fig. 17 presents the error history during refinement. This example yields conclusions similar to those above, demonstrating the feasibility of extending our method to three dimensions.

5.3. Linear elasticity problem

As mentioned in Remark 1, σ may map different sides of $\mathcal{P}$ to the same side of $\mathcal{Q}$. When solving the boundary value problem, if sides with distinct boundary conditions are mapped onto the same side, the corresponding boundary conditions will be inaccurately imposed. It is crucial to select an appropriate mapping σ.

To demonstrate the capabilities of the proposed method, we consider the linear elasticity problem, as illustrated in Fig. 18(a). The pentagonal computational domain in this example represents a flattened cross-section of an iron, with a downward traction uniformly applied to the top boundary while the bottom boundary is fixed. Fig. 18(b) depicts the bijective transformation between the parametric domains used in the MS-GIFT, where $\partial\mathcal{P}_N$ and $\partial\mathcal{Q}_N$ denote the corresponding boundaries of $\partial\Omega_N$ in the parametric domains. Figs. 18(c)–18(d) display the toric and NURBS parameterizations divided into 3 patches.

Since the linear elasticity problem is a more complex vector-valued field problem, finding an exact solution is challenging. Instead, we use the NURBS solutions with abundant DOFs as a reference. Fig. 19 presents a comparison of the numerical solutions obtained by the
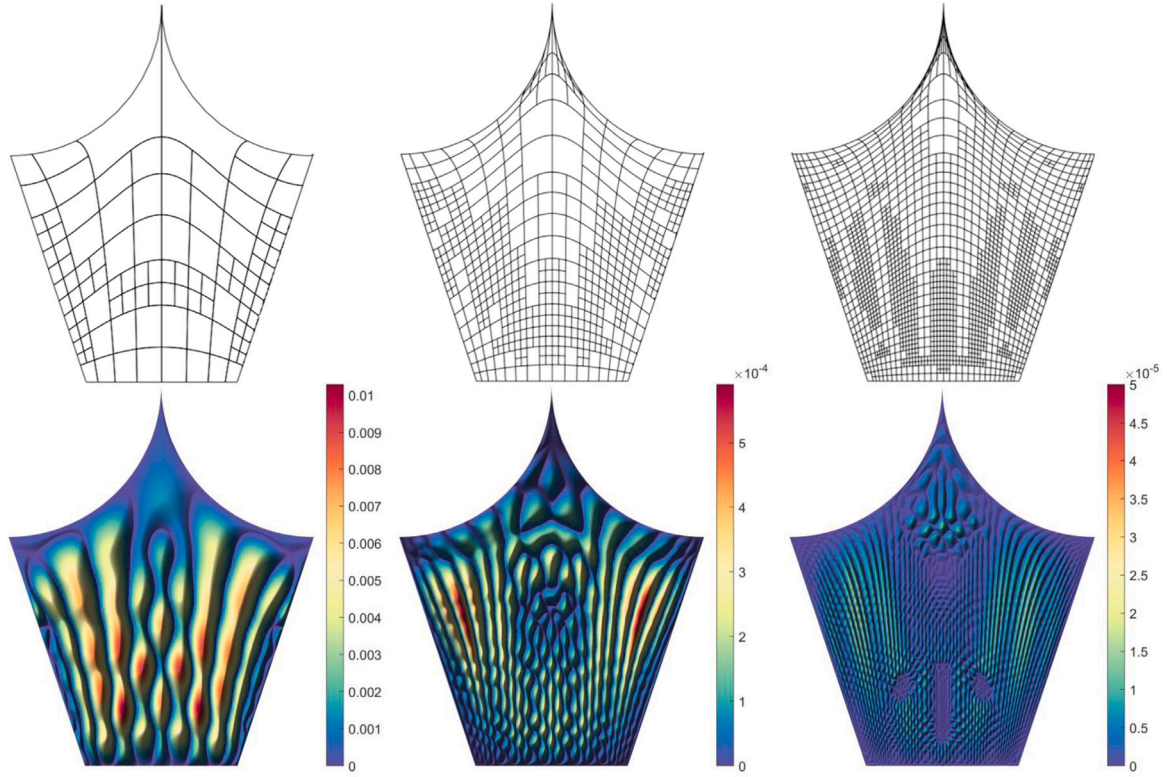
Fig. 13. Adaptive meshes (top) at steps 6, 10, 13 and corresponding absolute error colormaps (bottom) with DOFs 130, 346, 1369 by MS-GIFT (from left to right). (For interpretation of the references to color in this figure legend, the reader is referred to the web version of this article.)
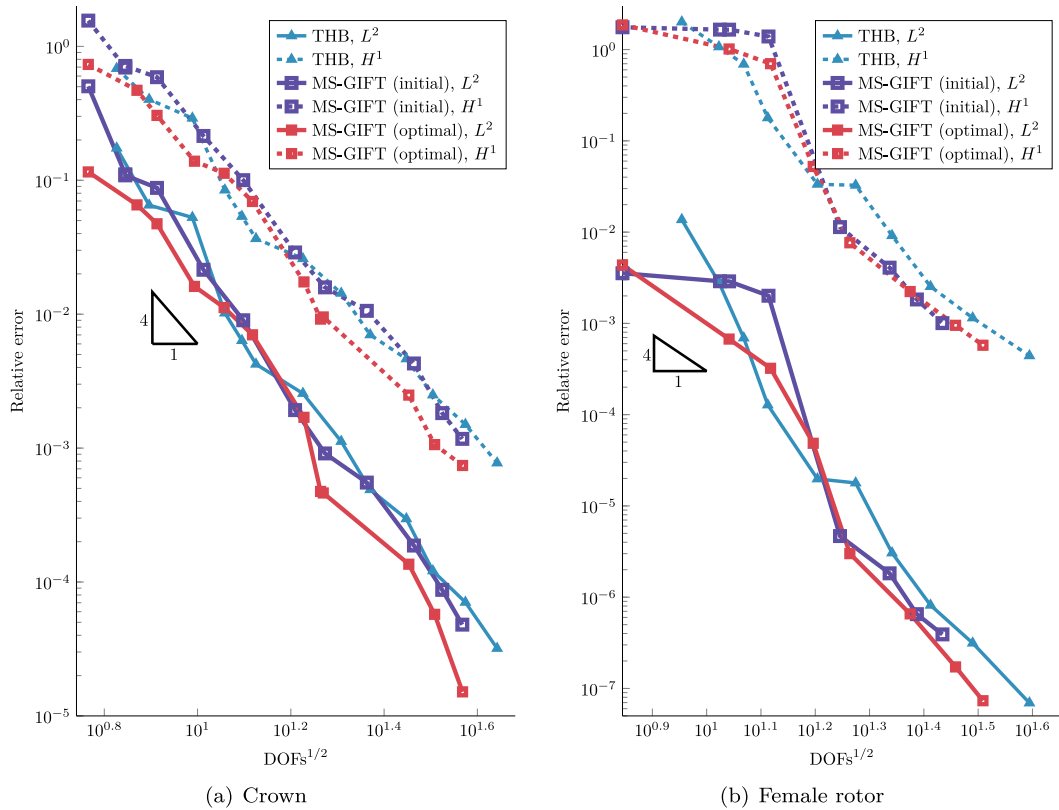

(a) Crown
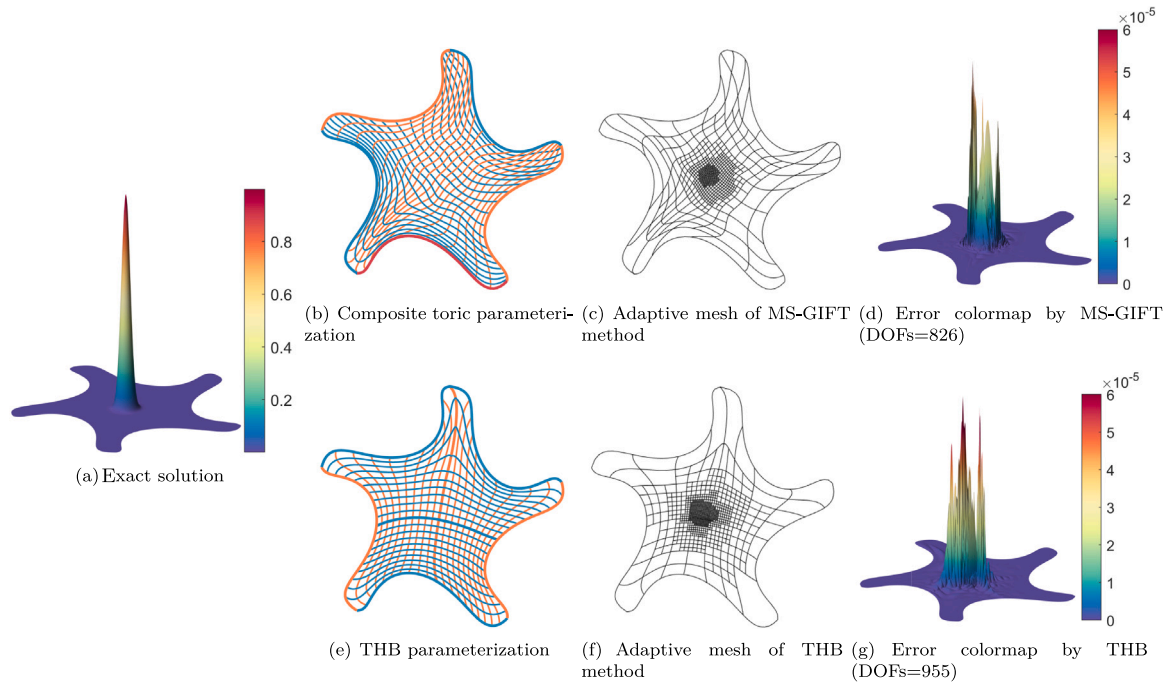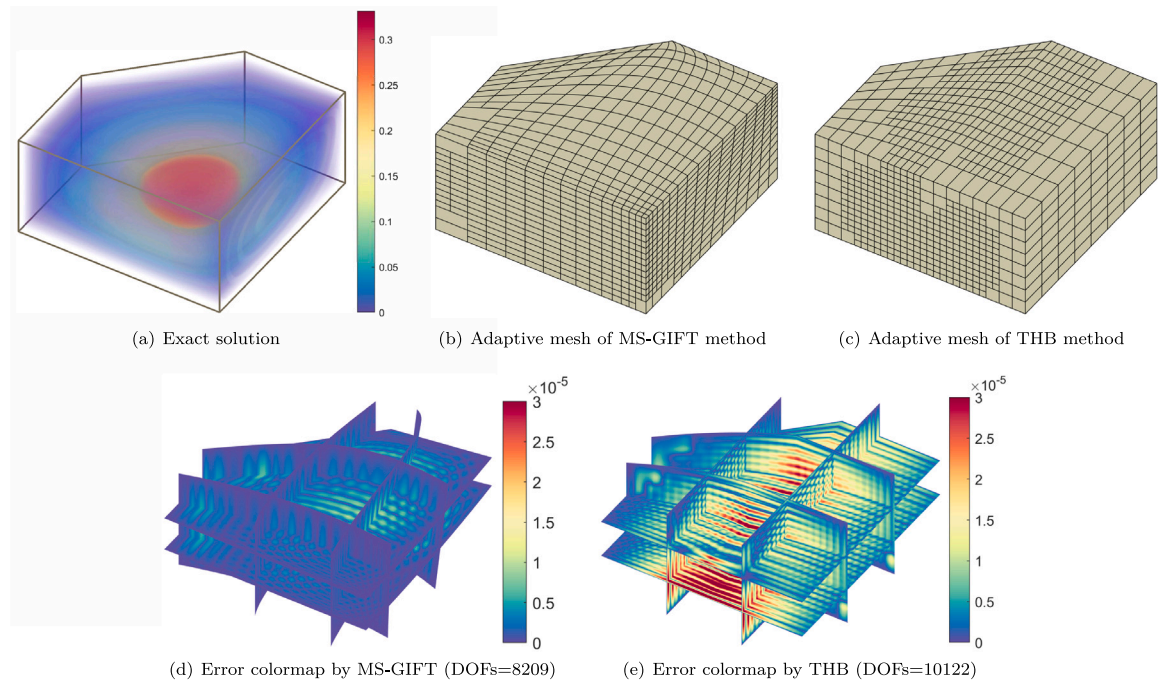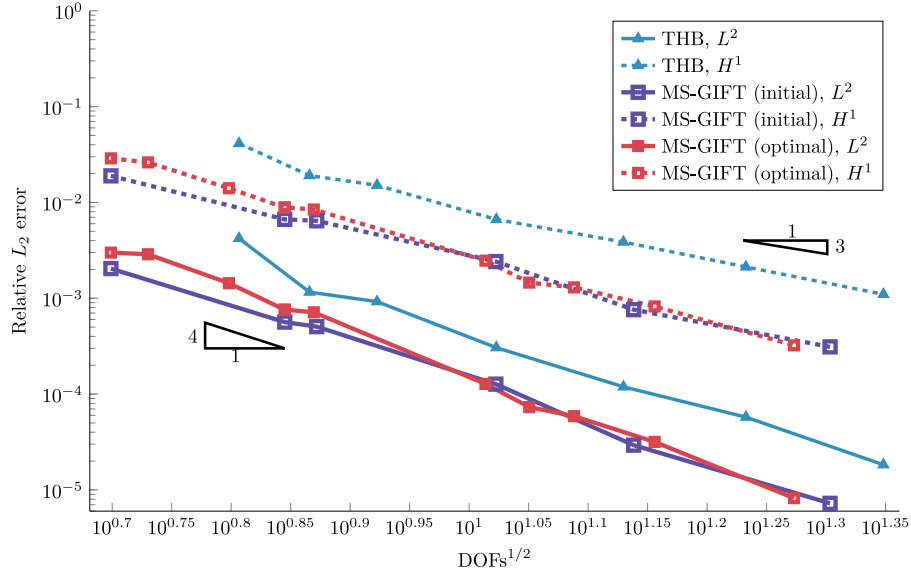
(b) Female rotor

Fig. 14. Error history during adaptive refinement. (For interpretation of the references to color in this figure legend, the reader is referred to the web version of this article.)

(a) Exact solution

(b) Composite toric parameterization

(c) Adaptive mesh of MS-GIFT method

(d) Error colormap by MS-GIFT (DOFs=826)

(e) THB parameterization

(f) Adaptive mesh of THB method

(g) Error colormap by THB (DOFs=955)

Fig. 15. Female rotor: a pentagonal computational domain.

(a) Exact solution

(b) Adaptive mesh of MS-GIFT method

(c) Adaptive mesh of THB method

(d) Error colormap by MS-GIFT (DOFs=8209)

(e) Error colormap by THB (DOFs=10122)

Fig. 16. Pentagonal prism: a 2.5-D domain. (For interpretation of the references to color in this figure legend, the reader is referred to the web version of this article.)

Fig. 17. Pentagonal prism: Error history during refinement.

(a) Problem description

(b) The bijection between parametric domains

(c) composite toric parameterization

(d) NURBS parameterization
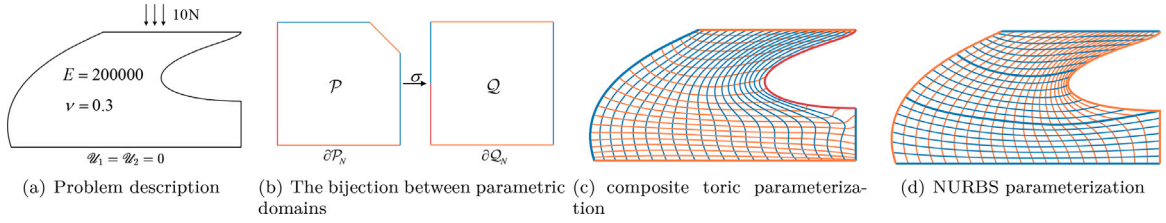
Fig. 18. Iron: a pentagonal computational domain.

(a) Vertical displace ($\mathscr{U}_2$)

(b) Principal stress (σ_x)

(c) Principal stress (σ_y)
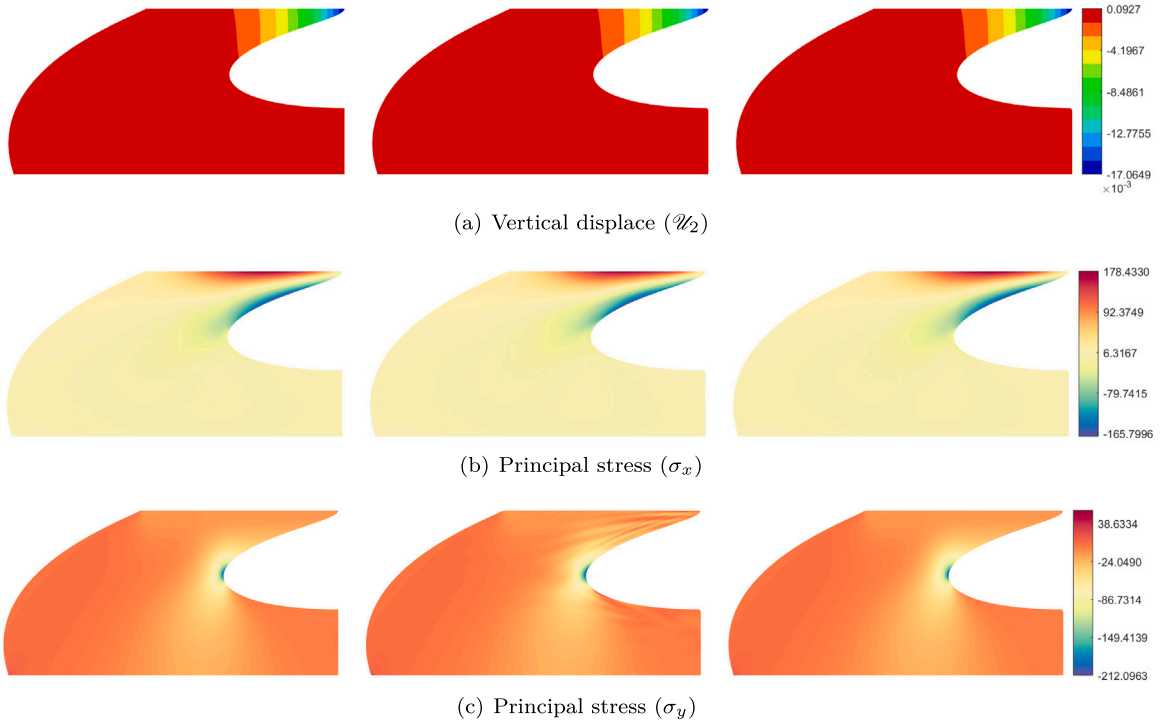
Fig. 19. The first column: NURBS over-killed solution (DOFs = 69432); the second column: MS-GIFT solution (DOFs = 760); the last column: MS-GIFT solution (DOFs = 4760)
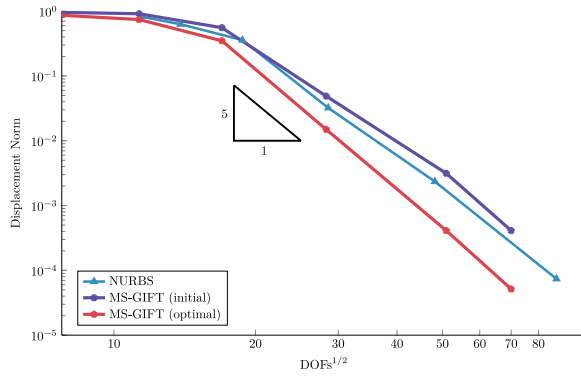
(a) Displacement norm error during refinement
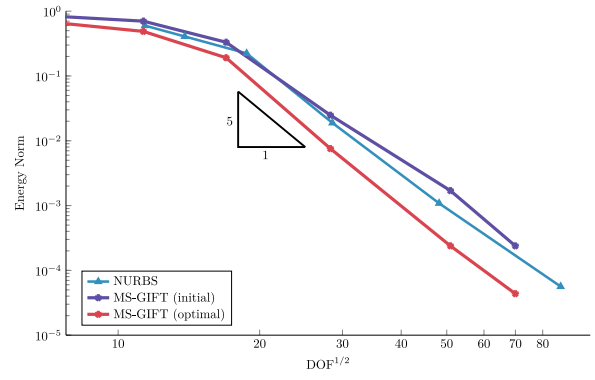
(b) Energy norm error during refinement

Fig. 20. Iron: error history of displacement norm error (left) and energy norm error (right)

NURBS over-killed method (DOFs = 69432) and the proposed method (DOFs = 760, 4760). As the DOFs increase, we observe that the numerical solutions become closer to the over-killed solutions. Fig. 20 provides the error history of displacement norm and energy norm, illustrating the superiority of our method.

6. Conclusions and future work

In this paper, we present a novel extension of IGA based on GIFT, named MS-GIFT, that employs toric surface patches to represent multi-sided geometry while utilizing B-spline or THB-spline basis functions for analysis. The MS-GIFT method ensures smoothness within the polygonal computational domain and incorporates locality in the solution basis, resulting in more efficient and accurate solutions. Moreover, we propose the optimization of composite toric parameterization to tackle the issue of non-uniform elements arising from the bijective mapping between the parametric domains of toric geometry and analysis basis functions. Numerical examples showcase that our method is better suited for IGA involving multi-sided geometries.

We anticipate addressing the following potential improvements in future work:

(1) Addressing computational domains of increased complexity: A notable constraint of the MS-GIFT approach is its applicability predominantly to convex, multi-sided geometrical domains. Incorporating the harmonic functions and utilizing advanced multi-patch configurations can be a promising extension of the proposed method. This enhancement would facilitate the MS-GIFT approach on domains with concave corners as well as those including higher-genus topologies.

(2) Developing three-dimensional composite toric parameterization for convex polyhedra. Although Wachspress barycentric coordinates have been extended to three dimensions [36], building a bijective mapping between the unit cube and convex polyhedra still presents a significant challenge.

(3) Examining the boundaries of toric surface patches as NURBS curves. In practical applications, NURBS-based representations offer more flexibility and are more common. Consequently, developing a MS-GIFT method based on NURBS-based B-Rep is interesting.

CRediT authorship contribution statement

Meng-Yun Wang: Writing – review & editing, Writing – original draft, Visualization, Validation, Methodology, Formal analysis, Data curation, Conceptualization. **Ye Ji:** Writing – review & editing, Writing – original draft, Visualization, Validation, Methodology, Formal analysis, Data curation, Conceptualization. **Lin Lan:** Writing – review & editing, Writing – original draft, Visualization, Formal analysis, Data curation, Conceptualization. **Chun-Gang Zhu:** Writing – review & editing, Writing – original draft, Visualization, Validation, Supervision, Resources, Project administration, Methodology, Investigation, Funding acquisition, Formal analysis, Conceptualization.

Declaration of competing interest

The authors declare that they have no known competing financial interests or personal relationships that could have appeared to influence the work reported in this paper.

Data availability

Data will be made available on request.

Appendix A. Manufactured solutions for numerical examples

For the numerical examples in Section 5, the boundaries and the manufactured solutions are as follows:

- **Strawberry** (Fig. 7).

$$C^1 = (x - y + 19)^2 - 4y + 56,$$
$$C^2 = x + y + 2(\frac{x}{4} + \frac{y}{2} - \frac{23}{4})^2 - 9,$$
$$C^3 = x - y - 2(\frac{x}{4} - \frac{y}{2} + \frac{23}{4})^2 + 9,$$
$$C^4 = \frac{x}{5} + \frac{2y}{5} - (\frac{x}{10} - \frac{3y}{10} + \frac{47}{10})^2 - \frac{28}{5}, \quad \text{(A.1)}$$
$$C^5 = 1728x^3 + 2160x^2 y - 15552x^2 + 900xy^2 - 12960xy + 125y^3 - 7884y^2 + 62208,$$
$$C^6 = -1728x^3 + 2160x^2 y - 15552x^2 - 900xy^2 + 12960xy + 125y^3 - 7884y^2 + 62208y.$$

The manufactured solution in Fig. 7 is

$$\mathscr{U}^{\text{exact}} = -10^{-16} \prod_{i=1}^{6} C^i. \quad \text{(A.2)}$$

- **Bottle** (Fig. 10).

$$C^1 = (\frac{3}{4}x + \frac{1}{4}y - 1)^2 - (x - y),$$

$$C^2 = (x - \frac{x+y-5}{4} - 1)^2 - (x + y - 5), \tag{A.3}$$

$$C^3 = x, \quad C^4 = y - 1, \quad C^5 = y - 4,$$

$$C^6 = y, \quad C^7 = y - 5, \quad C^8 = x - 10.$$

The manufactured solution in Fig. 10 is

$$\mathscr{U}^{\text{exact}} = 10^{-4} \prod_{i=1}^{8} C^i. \tag{A.4}$$

- **Crown** (Fig. 12).

$$C^1 = \sin(3x + y + 6), \quad C^2 = \sin(3x - y - 6),$$

$$C^3 = (x + 2)^2 + (y - 2)^2 - 4,$$

$$C^4 = (x - 2)^2 + (y - 2)^2 - 4, \tag{A.5}$$

$$C^5 = \sin(y + 3).$$

The manufactured solution in Fig. 12 is

$$\mathscr{U}^{\text{exact}} = 10^{-3} \prod_{i=1}^{5} C^i. \tag{A.6}$$

- **Female rotor** (Fig. 15).
The manufactured solution in Fig. 15 is

$$\mathscr{U}^{\text{exact}} = e^{-10^5((x-0.09)^2 + y^2)}. \tag{A.7}$$

- **Pentagonal prism** (Fig. 16)

$$S^1 = x, \quad S^2 = y, \quad S^3 = z, \quad S^4 = 2 - x,$$

$$S^5 = 2 - y, \quad S^6 = 1 - z, \quad S^7 = 3 - x - y. \tag{A.8}$$

The manufactured solution in Fig. 16 is

$$\mathscr{U}^{\text{exact}} = \prod_{i=1}^{7} S^i. \tag{A.9}$$

Appendix B. Degree specifics of the spline configurations employed for analysis

Example	Degree
Strawberry (Fig. 7)	(3, 3)
Bottle (Fig. 10)	(2, 2)
Crown (Fig. 12)	(2, 2)
Female rotor (Fig. 15)	(2, 2)
Pentagonal prism (Fig. 16)	(3, 3, 3)
Iron (Fig. 18)	(4, 4)

References

[1] Hughes TJ, Cottrell JA, Bazilevs Y. Isogeometric analysis: CAD, finite elements, NURBS, exact geometry and mesh refinement. Comput Methods Appl Mech Engrg 2005;194(39–41):4135–95.

[2] Cottrell JA, Hughes TJ, Bazilevs Y. Isogeometric analysis: Toward integration of CAD and FEA. John Wiley & Sons; 2009.

[3] Wang S, Ren J, Fang X, Lin H, Xu G, Bao H, et al. IGA-suitable planar parameterization with patch structure simplification of closed-form polysquare. Comput Methods Appl Mech Engrg 2022;392:114678.

[4] Chen L, Xu G, Wang S, Shi Z, Huang J. Constructing volumetric parameterization based on directed graph simplification of l1 polycube structure from complex shapes. Comput Methods Appl Mech Engrg 2019;351:422–40.

[5] Toshniwal D, Hughes TJ. Isogeometric discrete differential forms: Non-uniform degrees, Bézier extraction, polar splines and flows on surfaces. Comput Methods Appl Mech Engrg 2021;376:113576.

[6] Cohen E, Martin T, Kirby R, Lyche T, Riesenfeld R. Analysis-aware modeling: Understanding quality considerations in modeling for isogeometric analysis. Comput Methods Appl Mech Engrg 2010;199(5–8):334–56.

[7] Xu G, Li M, Mourrain B, Rabczuk T, Xu J, Bordas SP. Constructing IGA-suitable planar parameterization from complex CAD boundary by domain partition and global/local optimization. Comput Methods Appl Mech Engrg 2018;328:175–200.

[8] Wang S, Ren J, Fang X, Lin H, Xu G, Bao H, et al. IGA-suitable planar parameterization with patch structure simplification of closed-form polysquare. Comput Methods Appl Mech Engrg 2022;392:114678.

[9] Zhang Y, Ji Y, Zhu C-G. Multi-patch parameterization method for isogeometric analysis using singular structure of cross-field. Comput Math Appl 2024;162:61–78.

[10] Wang D, Xu J, Gao F, Wang CC, Gu R, Lin F, et al. IGA-reuse-NET: A deep-learning-based isogeometric analysis-reuse approach with topology-consistent parameterization. Comput Aided Geom Design 2022;95:102087.

[11] Pan Q, Chen C, Rabczuk T, Zhang J, Yang X. The subdivision-based IGA-EIEQ numerical scheme for the binary surfactant Cahn–Hilliard phase-field model on complex curved surfaces. Comput Methods Appl Mech Engrg 2023;406:115905.

[12] Pan Q, Chen C, Zhang YJ, Yang X. A novel hybrid IGA-EIEQ numerical method for the Allen–Cahn/Cahn–Hilliard equations on complex curved surfaces. Comput Methods Appl Mech Engrg 2023;404:115767.

[13] Xie J, Xu J, Dong Z, Xu G, Deng C, Mourrain B, et al. Interpolatory Catmull-Clark volumetric subdivision over unstructured hexahedral meshes for modeling and simulation applications. Comput Aided Geom Design 2020;80:101867.

[14] Xu G, Li B, Shu L, Chen L, Xu J, Khajah T. Efficient r-adaptive isogeometric analysis with Winslow's mapping and monitor function approach. J Comput Appl Math 2019;351:186–97.

[15] Ji Y, Li J-G, Yu Y-Y, Zhu C-G. h-Refinement method for toric parameterization of planar multi-sided computational domain in isogeometric analysis. Comput Aided Geom Design 2022;93:102065.

[16] Wang M, Ji Y, Zhu C. Degree elevation and knot insertion for generalized Bézier surfaces and their application to isogeometric analysis. J Comput Math 2023.

[17] Krasauskas R. Toric surface patches. Adv Comput Math 2002;17:89–113.

[18] García-Puente LD, Sottile F, Zhu C. Toric degenerations of Bézier patches. ACM Trans Graph 2011;30(5):110.

[19] Yu Y-Y, Ji Y, Zhu C-G. An improved algorithm for checking the injectivity of 2D toric surface patches. Comput Math Appl 2020;79(10):2973–86.

[20] Zhu X, Ji Y, Zhu C, Hu P, Ma Z-D. Isogeometric analysis for trimmed CAD surfaces using multi-sided toric surface patches. Comput Aided Geom Design 2020;79:101847.

[21] Li J-G, Ji Y, Zhu C-G. De Casteljau algorithm and degree elevation of toric surface patches. J Syst Sci Complex 2021;34(1):21–46.

[22] Atroshchenko E, Tomar S, Xu G, Bordas SP. Weakening the tight coupling between geometry and simulation in isogeometric analysis: From sub-and super-geometric analysis to geometry-independent field approximation (GIFT). Internat J Numer Methods Engrg 2018;114(10):1131–59.

[23] Ma S, Xu J, Xu G. Fast isogeometric method for fluid–structure interaction simulation of heart valves with GIFT framework. Commun Math Stat 2023.

[24] Giannelli C, Jüttler B, Speleers H. THB-splines: The truncated basis for hierarchical splines. Comput Aided Geom Design 2012;29(7):485–98.

[25] Giannelli C, Jüttler B, Kleiss SK, Mantzaflaris A, Simeon B, Špeh J. THB-splines: An effective mathematical technology for adaptive refinement in geometric design and isogeometric analysis. Comput Methods Appl Mech Engrg 2016;299:337–65.

[26] Wachspress EL. A rational finite element basis. New York: Academic Press; 1975.

[27] Floater MS. Wachspress and mean value coordinates. In: Approximation theory XIV: san antonio 2013. Springer; 2014, p. 81–102.

[28] Xu G, Mourrain B, Duvigneau R, Galligo A. Optimal analysis-aware parameterization of computational domain in 3D isogeometric analysis. Comput Aided Des 2013;45(4):812–21.

[29] Pilgerstorfer E, Jüttler B. Bounding the influence of domain parameterization and knot spacing on numerical stability in isogeometric analysis. Comput Methods Appl Mech Engrg 2014;268:589–613.

[30] Floater M. One-to-one piecewise linear mappings over triangulations. Math Comp 2003;72(242):685–96.

[31] Várady T, Salvi P, Karikó G. A multi-sided Bézier patch with a simple control structure. Comput Graph Forum 2016;35(2):307–17.

[32] Ji Y, Yu Y-Y, Wang M-Y, Zhu C-G. Constructing high-quality planar NURBS parameterization for isogeometric analysis by adjustment control points and weights. J Comput Appl Math 2021;396:113615.

[33] Vázquez R. A new design for the implementation of isogeometric analysis in octave and matlab: GeoPDEs 3.0. Comput Math Appl 2016;72(3):523–54.

[34] Jüttler B, Langer U, Mantzaflaris A, Moore SE, Zulehner W. Geometry + simulation modules: Implementing isogeometric analysis. PAMM 2014;14(1):961–2.

[35] Geometry + simulation modules (G+Smo) v23.12. 2024, URL https://github.com/gismo/gismo. [Accessed 13 May 2024].

[36] Floater M, Gillette A, Sukumar N. Gradient bounds for Wachspress coordinates on polytopes. SIAM J Numer Anal 2014;52(1):515–32.